mathematics

MDPI

Article

Platform-Motion Response Evolution and Predicted TDB-Clearance Risk of a Ship-Mounted Flexible Rotor–Active Magnetic Bearing System

Houxiang Wang [1,†], Zhuo Wang [2,†], Wencai Sun [1,*], Lingfeng Hu [1] and Xingyu Wang [1]

[1] Naval University of Engineering, Wuhan 430033, China; x22182708@nue.edu.cn (H.W.); m24380704@nue.edu.cn (L.H.); m25185802@nue.edu.cn (X.W.)
[2] Huazhong University of Science and Technology, Wuhan 430033, China; wz0716@hust.edu.cn
* Correspondence: m22170101@nue.edu.cn
† These authors contributed equally to this work.

Abstract

Platform motion alters the flexible response and control demand of ship-mounted rotor–active magnetic bearing (AMB) systems and thereby the clearance margin at the touchdown bearings (TDBs). A closed-loop finite-element model of a flexible rotor–AMB system is subjected to prescribed heave, sway, pitch, and yaw motions at five rotational speeds and 4×4 amplitude–frequency levels (320 cases). Responses are evaluated at the TDBs, the disk, and 36 axial positions, together with the AMB control force and the ratio of peak TDB displacement to minimum clearance, assessed against the ISO 14839-2 zones. Stronger excitation increases the support and disk responses and moves the axial response peak; each platform motion has its own dominant direction and left–right support relation. Ten cases, all high-amplitude, high-frequency heave or sway, enter zone D; the maximum clearance ratio is 0.635, and its correlation with the maximum control force is 0.9995. A closed-form envelope derived from the closed-loop dynamic stiffness reproduces the simulated ratios and shows that the zone boundaries are set by the platform acceleration amplitude: zone D requires 4.9–7.1 g under heave or sway. The disk displacement peaks at 2500 rpm, whereas the control force and clearance ratio peak at 7000 rpm, so deformation, control demand, and clearance margin have to be assessed together.

Keywords: active magnetic bearing; prescribed platform motion; axial flexible response; AMB control demand; TDB clearance

MSC: 74H45

Check for updates

Academic Editors: Lei Li, Linchuan Zhao and Yuqi Li

Received: 21 September 2026
Revised: 22 October 2026
Accepted: 25 October 2026
Published: 28 October 2026

Copyright: © 2026 by the authors. Licensee MDPI, Basel, Switzerland. This article is an open access article distributed under the terms and conditions of the Creative Commons Attribution (CC BY) license.

1. Introduction

Shipboard turbine generators, compressors, and flywheel energy-storage units are high-speed rotating machines that operate for long periods in a non-inertial environment in which the supporting base continuously translates and rotates. Active magnetic bearings (AMBs) provide contactless support, adjustable stiffness and damping, and built-in state sensing, and are widely used to levitate flexible rotors and suppress their vibration [1,2]. The electromagnetic force of an AMB is limited, however, so the system must include touchdown bearings (TDBs) whose radial clearance is only a fraction of a millimeter. If platform motion drives the displacement at a support section beyond this clearance, the rotor contacts the TDB, which causes impacts, frictional heating, backward whirl, and even

loss of levitation. For an AMB–rotor system on a moving platform, the vibration amplitude alone is therefore not sufficient: the transmission of platform excitation along the flexible rotor, the AMB control demand, and the margin to the protective clearance must also be determined. These quantities are coupled through the closed loop and cannot be inferred directly from fixed-base analyses.

Rotor dynamics under base motion has been studied for different bearing types, platform motions, and control strategies. Base motion can induce parametric excitation and change the steady-state response and control demand of a flexible rotor [3,4], and the rotor response and control cost depend strongly on sea state and control strategy [5]. For marine rotating machinery, the effects of pitch, roll, heave, and their combinations on shaft-center orbits, bifurcations, and stability regions have been examined in detail [6–13]. Most of these studies, however, concern hydrodynamic bearings and report responses at the disk or bearing locations. Because the support characteristics of an AMB are set by the feedback controller and are strongly frequency dependent, these results cannot be transferred directly to AMB-supported rotors.

For AMB-supported rotors, parametric stability under base motion, dynamic modeling, and the vibration response of flexible rotors have been investigated [14–16]. Base motion enters the closed-loop dynamics through additional inertial forces, additional stiffness, and gyroscopic effects. On the control side, disturbance observers have been used to suppress vibration caused by base motion [17], and the elastic modes of a flexible rotor and the actuator layout have to be treated together in closed-loop modeling [18,19]. Recent experiments on a six-degree-of-freedom shaking table and in a ship-model towing tank have quantified the effect of base rocking and hull excitation on rotor–bearing systems [20,21], and the periodic stability of rotors with squeeze-film dampers under base motion has been analyzed [22]. AMBs have also been used to control the vibration of base-excited rotors [23,24] and of magnetic-bearing flywheels on moving bases [25]. Existing work, however, concentrates on stability boundaries or controller design. How the type of platform motion and its amplitude and frequency affect the axial response distribution of a flexible rotor, the relation between the left and right supports, and the control demand has not been compared systematically.

Research on touchdown bearings has covered rub modeling and experiments for ship-mounted rotor–AMB systems [26], synchronous contact and position-recovery control [27,28], rotor-drop transients [29,30], thermal growth [31,32], multiple sliding and rolling contacts [33], bearing misalignment [34], and contact-force measurement and control of persistent synchronous contact [35,36]. These studies describe the dynamics after contact. The stage before contact, in which platform motion brings the rotor towards the clearance limit, decides whether contact occurs; its assessment is needed to design the protective clearance, size the actuators, and define a safe operating envelope for shipboard AMB machinery.

Three gaps therefore remain: (1) the axial evolution of the flexible-rotor response and the asymmetry between the left and right supports under different platform motions have rarely been resolved in a closed-loop AMB model; (2) there is no systematic mapping between platform-motion parameters and a TDB clearance index, so the clearance-critical conditions are not known; and (3) displacement, control force, and clearance margin are usually evaluated separately, and it is unclear whether their worst cases coincide.

This study builds a closed-loop finite-element model of a flexible rotor–AMB system under heave, sway, pitch, and yaw, and analyzes 320 cases formed by four motion types, five rotational speeds, and 4×4 amplitude–frequency levels. The novelty lies in three aspects:

1. Full-shaft response under platform motion. The response consists of a quasi-static platform deflection with a nearly unchanged axial shape superposed on the syn-

chronous unbalance orbit. As the platform contribution increases, the dominant support switches from right to left and the axial hotspot moves, showing why assessment at a single location may miss the critical section.

2. Closed-form clearance-zone boundaries. A TDB displacement envelope derived from the closed-loop dynamic stiffness gives the ISO 14839-2 zone boundaries explicitly as hyperbolae $\alpha\beta^2 = \text{const}$ and a critical platform acceleration of 4.9–7.1 g for zone D under heave or sway. The envelope reproduces the 320 simulations with $R^2 = 0.997$.
3. Joint assessment of deformation, control demand, and clearance margin. The disk displacement peaks at 2500 rpm, whereas the control force and λ_D peak at 7000 rpm; the control force follows λ_D with $r = 0.9995$ and can serve as an indirect indicator of the clearance margin.

Section 2 presents the rotor–AMB model and its validation, Section 3 defines the evaluation metrics and derives the closed-form TDB envelope, Section 4 discusses the results, and Section 5 concludes the paper.

2. Numerical Model and Time-Domain Solution

2.1. System Configuration and Coordinate System

Figure 1 shows the ship-mounted flexible rotor–active magnetic bearing system and the platform coordinate system considered in this study. The system mainly comprises a flexible rotor, motor, disk, two radial AMBs on the left and right, and the corresponding displacement sensors. The rotor system is installed on a moving platform. The axial coordinate of the rotor is denoted by z, and the transverse directions are denoted by x and y, with corresponding displacements $u_x(z,t)$ and $u_y(z,t)$.

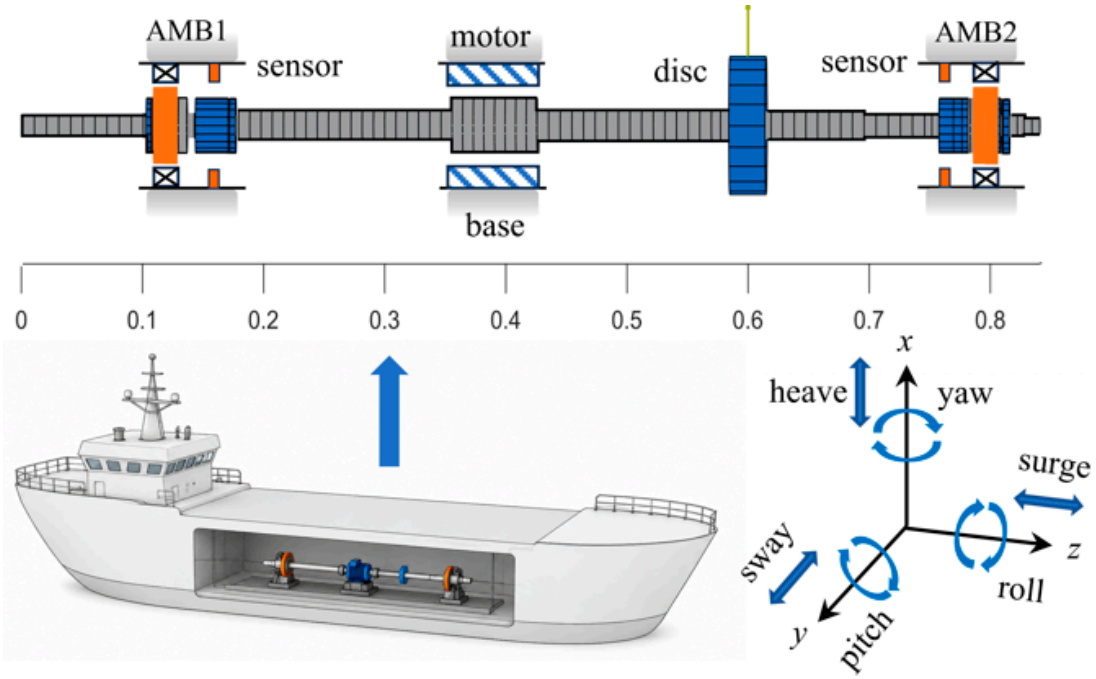


Figure 1. Schematic of the ship-mounted flexible rotor–active magnetic bearing system and the platform-motion coordinate system.

The six-degree-of-freedom motion vector of the platform is defined as

$$\vec{\eta}_b(t) = \begin{bmatrix} x_b(t) & y_b(t) & z_b(t) & \phi_b(t) & \theta_b(t) & \psi_b(t) \end{bmatrix}^{\mathrm{T}} \tag{1}$$

The parameter scan activates one degree of freedom in each case and includes four types of platform motion: heave, sway, pitch, and yaw. Three key axial sections, the left AMB, disk, and right AMB, are defined at z_{L}, z_{D}, and z_{R}, respectively. The left and right TDBs are co-located with the corresponding AMB sections, where

$$z_{\mathrm{L}} \approx 0.113 \text{ m}, \; z_{\mathrm{R}} \approx 0.800 \text{ m} \tag{2}$$

The flexible rotor is represented by a linear finite-element model, the AMB electromagnetic force is linearized near the operating point, and a linear PID controller is used. Platform motion enters the rotor dynamics through equivalent inertial loads in a body-fixed non-inertial coordinate system. The TDB clearance state is mapped from the radial displacements at the left and right support positions.

2.2. Finite-Element Model of the Flexible Rotor

The flexible rotor is axially discretized into two-node Timoshenko beam elements, with corresponding nodes placed at the disk and support positions. Each node has six degrees of freedom, and the disk is assembled in the form of concentrated mass and rotary inertia. The model accounts for rotor bending, disk inertia, and rotational-speed-dependent gyroscopic coupling [37–42]. The global generalized coordinate is denoted by

$$\mathbf{q}(t) = \begin{bmatrix} q_1(t) & q_2(t) & \cdots & q_{n_q}(t) \end{bmatrix}^{\mathrm{T}} \tag{3}$$

The local degrees of freedom of the eth beam element are extracted using the assembly matrix $\mathbf{A}_e$:

$$\mathbf{q}_e(t) = \mathbf{A}_e \mathbf{q}(t) \tag{4}$$

The transverse displacement and cross-sectional rotation within the element are expressed as

$$\mathbf{u}_e(z,t) = \mathbf{N}_u(z)\mathbf{q}_e(t) \tag{5}$$

$$\vec{\vartheta}_e(z,t) = \mathbf{N}_\vartheta(z)\mathbf{q}_e(t) \tag{6}$$

The mass and stiffness matrices are obtained from the element kinetic and strain energies, respectively, and have the general forms

$$\mathbf{M}_e = \int_{V_e} \rho \mathbf{N}^{\mathrm{T}} \mathbf{N} \mathrm{d}V \tag{7}$$

$$\mathbf{K}_e = \int_{V_e} \mathbf{B}^{\mathrm{T}} \mathbf{D} \mathbf{B} \mathrm{d}V \tag{8}$$

Timoshenko beam elements are used because they include shear deformation and rotary inertia, are consistent with the gyroscopic matrix, and reduce to Euler–Bernoulli elements as the shear parameter vanishes [39,41]. Shear deformation enters through $\Phi_e = 12EI_e/(k_{sc}GA_e l_e^2)$ with $G = E/[2(1+\nu)]$, where the shear coefficient of the solid circular section is $k_{sc} = 6(1+\nu)/(7+6\nu) = 0.886$ ($\nu = 0.30$). The rotor is slender ($L/D \approx 37$), and Euler–Bernoulli elements would change the first three bending frequencies by less than 0.6%; the Timoshenko formulation is kept for the short elements at the disk and the stepped bearing sections.

The disk is assembled as concentrated mass and a concentrated gyroscopic matrix. The global mass, stiffness, and gyroscopic matrices are

$$\mathbf{M} = \sum_{e=1}^{n_e} \mathbf{A}_e^{\mathrm{T}} \mathbf{M}_e \mathbf{A}_e + \sum_{d=1}^{n_d} \mathbf{M}_d \tag{9}$$

$$\mathbf{K} = \sum_{e=1}^{n_e} \mathbf{A}_e^{\mathrm{T}} \mathbf{K}_e \mathbf{A}_e \tag{10}$$

$$\mathbf{G} = \sum_{e=1}^{n_e} \mathbf{A}_e^{\mathrm{T}} \mathbf{G}_e \mathbf{A}_e + \sum_{d=1}^{n_d} \mathbf{G}_d \tag{11}$$

Structural damping is represented in Rayleigh form as

$$\mathbf{C}_{\mathrm{r}} = \alpha_1 \mathbf{K}_{\mathrm{r}} + \alpha_2 \mathbf{M}_{\mathrm{r}} \tag{12}$$

where $\alpha_1 = 5 \times 10^{-7}$ s and $\alpha_2 = 0$. For a specified rotational speed n, the angular velocity is

$$\Omega = \frac{2\pi n}{60} \tag{13}$$

The transverse load generated by the uth unbalance source is

$$\mathbf{f}_u(t) = m_u e_u \Omega^2 \begin{bmatrix} \cos(\Omega t + \varphi_u) \\ \sin(\Omega t + \varphi_u) \end{bmatrix} \tag{14}$$

Its globally assembled form is

$$\mathbf{F}_{\mathrm{ub}}(t) = \sum_{u=1}^{n_u} \mathbf{S}_u^{\mathrm{T}} \mathbf{f}_u(t) \tag{15}$$

The basic finite-element equation of the flexible rotor under the synchronous unbalance load of Equation (15) is written as

$$\mathbf{M}\ddot{\mathbf{q}} + (\mathbf{C} + \Omega \mathbf{G})\dot{\mathbf{q}} + \mathbf{K}\mathbf{q} = \mathbf{F}_{\mathrm{ub}} \tag{16}$$

2.3. Platform Motion and Non-Inertial Base Coupling

For the activated platform degree of freedom, the prescribed motion is harmonic:

$$q_b(t) = A_b \sin(\omega_b t + \varphi_b) \tag{17}$$

$$\dot{q}_b(t) = A_b \omega_b \cos(\omega_b t + \varphi_b) \tag{18}$$

$$\ddot{q}_b(t) = -A_b \omega_b^2 \sin(\omega_b t + \varphi_b) \tag{19}$$

where $\omega_b = 2\pi f_b$. The amplitude and frequency scans are implemented through

$$A_b = a_s A_{b,0},\ f_b = f_s f_{b,0},\ a_s, f_s \in \{1, 2, 3, 4\} \tag{20}$$

Let the platform reference point be O_b. The position of the ith rotor node relative to this point is

$$\mathbf{r}_i = \begin{bmatrix} 0 & 0 & z_i \end{bmatrix}^{\mathrm{T}} \tag{21}$$

In the platform-fixed non-inertial coordinate system, the equivalent nodal acceleration is based on the standard kinematic relation for a rigid-body reference frame [43]:

$$\mathbf{a}_{i,\mathrm{eq}} = \mathbf{a}_b + \dot{\vec{\omega}}_b \times \mathbf{r}_i + \vec{\omega}_b \times \left(\vec{\omega}_b \times \mathbf{r}_i \right) + 2\vec{\omega}_b \times \mathbf{v}_{i,\mathrm{rel}} + \Delta \mathbf{g}_i \tag{22}$$

The equivalent nodal inertial force is

$$\mathbf{f}_{i,\mathrm{base}} = -m_i \mathbf{a}_{i,\mathrm{eq}} \tag{23}$$

The global platform-equivalent load is

$$\mathbf{F}_{\text{base}}(t) = -\sum_{i=1}^{n_n} \mathbf{S}_i^{\mathrm{T}} m_i \mathbf{a}_{i,\text{eq}}(t) \tag{24}$$

Equation (22) contains platform translation, Euler, centrifugal, Coriolis, and gravity-projection terms caused by attitude changes. Under small-angle harmonic motion, heave and sway primarily generate transverse inertial loads that are approximately in phase along the axial direction. Through $\mathbf{r}_i$, the Euler terms for pitch and yaw generate distributed loads that depend on axial position. The platform is treated as a rigid body, so hull deformation is not included. Physically, the platform motion is a kinematic (support) excitation of the AMB stators and TDBs. Because the AMB position sensors and the TDB clearance refer to the rotor displacement relative to the stator, the equations are written in the platform-fixed frame, where the prescribed support motion appears exactly as the equivalent inertial load of Equation (24) and the generalized coordinate $\mathbf{q}$ is the rotor displacement relative to the platform. For a rigid platform the kinematic and the inertial descriptions are therefore equivalent.

2.4. AMB Electromagnetic Actuators and Closed-Loop Control Model

The system contains two radial AMBs on the left and right, and each support has independent feedback channels in the x and y directions [44–46]. The state at the jth AMB support is extracted from the global coordinates by the selection matrix $\mathbf{S}_j$:

$$\mathbf{u}_j = \mathbf{S}_j \mathbf{q} \tag{25}$$

$$\dot{\mathbf{u}}_j = \mathbf{S}_j \dot{\mathbf{q}} \tag{26}$$

The error under a zero-displacement reference is

$$\mathbf{e}_j = -\mathbf{u}_j \tag{27}$$

The PID integral state is defined as

$$\dot{\vec{\xi}}_j = \mathbf{e}_j \tag{28}$$

The current command is written as

$$\mathbf{i}_{c,j} = \mathbf{K}_{P,j}\mathbf{e}_j + \mathbf{K}_{I,j}^{c}\vec{\xi}_j + \mathbf{K}_{D,j}\dot{\mathbf{e}}_j \tag{29}$$

The current–force relationship near the operating point is linearized as

$$\mathbf{f}_{\text{ctrl},j} = \mathbf{K}_{f,j}\mathbf{i}_{c,j},\ \mathbf{K}_{f,j} = k_{i,j}\mathbf{I}_2 \tag{30}$$

The support displacement stiffness is assembled as

$$\mathbf{K}_{x,\text{comp}} = \sum_{j\in\{\text{L,R}\}} \mathbf{S}_j^{\mathrm{T}} k_{x,j} \mathbf{I}_2 \mathbf{S}_j \tag{31}$$

The total AMB force includes the current-controlled electromagnetic force, with the current stiffness $k_{i,j}$ of Equation (30), and the linearized displacement-stiffness contribution, where $k_{x,j} < 0$ is the negative displacement stiffness of the magnet (Table 1):

$$\mathbf{F}_{\text{AMB}}(t) = \sum_{j\in\{\text{L,R}\}} \mathbf{S}_j^{\mathrm{T}} \left[\mathbf{f}_{\text{ctrl},j}(t) - k_{x,j}\mathbf{u}_j(t)\right] = \sum_{j\in\{\text{L,R}\}} \mathbf{S}_j^{\mathrm{T}} \mathbf{f}_{\text{ctrl},j}(t) - \mathbf{K}_{x,\text{comp}}\mathbf{q}(t) \tag{32}$$

Table 1. Main model and numerical parameters.

Category	Parameter	Value
Material	Elastic modulus E	220 GPa
Material	Density ρ	7860 kg/m^3
Material	Poisson's ratio ν	0.30
Left AMB	Axial position z_{L}	0.113 m
Right AMB	Axial position z_{R}	0.800 m
Controller	Type	Linear PID
Controller	Proportional gain K_P	8.6×10^3 A/m
Controller	Integral gain K_I^c	15 A/(ms)
Controller	Derivative gain K_D	3.8 As/m
AMB	Current–force coefficient k_i	148.8 N/A
AMB	Signed displacement stiffness k_x	-6.7×10^5 N/m
Rotor damping	Stiffness-proportional coefficient α_1	5×10^{-7} s
Rotor damping	Mass-proportional coefficient α_2	0
Other isotropic supports	Damping	10 Ns/m
Numerical integration	Newmark parameters	$\beta = 1/4$, $\gamma = 1/2$
Numerical integration	Total duration	3 s
Numerical integration	Time step	5×10^{-5} s
Numerical integration	Number of samples	60,001
Parameter scan	Rotational speed	1000, 2500, 4000, 5500, 7000 rpm
Parameter scan	Amplitude multiplier a_s	1, 2, 3, 4
Parameter scan	Frequency multiplier f_s	1, 2, 3, 4
Parameter scan	Total number of cases	320
Clearance metric	Minimum TDB radial clearance	$C_{\min} = 250$ μm

After the linear PID feedback is incorporated into the system matrices, the velocity, displacement, and integral feedback matrices are, respectively,

$$\mathbf{C}_{\mathrm{AMB}} = \sum_j \mathbf{S}_j^{\mathrm{T}} \mathbf{K}_{f,j} \mathbf{K}_{D,j} \mathbf{S}_j \tag{33}$$

$$\mathbf{K}_{\mathrm{AMB}} = \sum_j \mathbf{S}_j^{\mathrm{T}} \mathbf{K}_{f,j} \mathbf{K}_{P,j} \mathbf{S}_j \tag{34}$$

$$\mathbf{B}_{I,\mathrm{AMB}} = \begin{bmatrix} \mathbf{S}_{\mathrm{L}}^{\mathrm{T}} \mathbf{K}_{f,\mathrm{L}} \mathbf{K}_{I,\mathrm{L}}^c & \mathbf{S}_{\mathrm{R}}^{\mathrm{T}} \mathbf{K}_{f,\mathrm{R}} \mathbf{K}_{I,\mathrm{R}}^c \end{bmatrix} \tag{35}$$

This gives the equivalent closed-loop equation, in which the net static stiffness of each controlled direction is $k_i K_P + k_x \approx 6.1 \times 10^5$ N/m for the parameters of Table 1:

$$\mathbf{M}\ddot{\mathbf{q}} + (\mathbf{C} + \Omega\mathbf{G} + \mathbf{C}_{\mathrm{AMB}})\dot{\mathbf{q}} + \left(\mathbf{K} + \mathbf{K}_{\mathrm{AMB}} + \mathbf{K}_{x,\mathrm{comp}}\right)\mathbf{q} - \mathbf{B}_{I,\mathrm{AMB}}\vec{\xi} = \mathbf{F}_{\mathrm{ub}} + \mathbf{F}_{\mathrm{base}} \tag{36}$$

2.5. Complete Dynamic Equation and Time-Domain Integration

The time-domain calculation uses the original force-balance form

$$\mathbf{M}\ddot{\mathbf{q}} + (\mathbf{C} + \Omega\mathbf{G})\dot{\mathbf{q}} + \mathbf{K}\mathbf{q} = \mathbf{F}_{\mathrm{ub}} + \mathbf{F}_{\mathrm{base}} + \mathbf{F}_{\mathrm{AMB}} \tag{37}$$

A fixed-step Newmark–β average-acceleration scheme is used [47,48], with

$$\beta = \frac{1}{4},\ \gamma = \frac{1}{2} \tag{38}$$

The predicted displacement and velocity at time step $k+1$ are

$$\mathbf{q}_{k+1}^{*} = \mathbf{q}_k + \Delta t \dot{\mathbf{q}}_k + \left(\frac{1}{2} - \beta\right)\Delta t^2 \ddot{\mathbf{q}}_k \tag{39}$$

$$\dot{\mathbf{q}}_{k+1}^{*} = \dot{\mathbf{q}}_k + (1-\gamma)\Delta t\ddot{\mathbf{q}}_k \tag{40}$$

Let

$$\mathbf{C}_\Omega = \mathbf{C} + \Omega\mathbf{G} \tag{41}$$

The effective matrix is

$$\mathbf{S}_\mathrm{N} = \mathbf{M} + \gamma\Delta t\mathbf{C}_\Omega + \beta\Delta t^2\mathbf{K} \tag{42}$$

The total load at this step is

$$\mathbf{F}_{k+1}^{*} = \mathbf{F}_\mathrm{ub}(t_{k+1}) + \mathbf{F}_{\mathrm{base},k+1}^{*} + \mathbf{F}_{\mathrm{AMB},k+1}^{*} \tag{43}$$

The structural acceleration is obtained from

$$\ddot{\mathbf{q}}_{k+1} = \mathbf{S}_\mathrm{N}^{-1}\left[\mathbf{F}_{k+1}^{*} - \mathbf{C}_\Omega\dot{\mathbf{q}}_{k+1}^{*} - \mathbf{K}\mathbf{q}_{k+1}^{*}\right] \tag{44}$$

and the displacement and velocity are corrected using the Newmark update relations:

$$\mathbf{q}_{k+1} = \mathbf{q}_{k+1}^{*} + \beta\Delta t^2\ddot{\mathbf{q}}_{k+1} \tag{45}$$

$$\dot{\mathbf{q}}_{k+1} = \dot{\mathbf{q}}_{k+1}^{*} + \gamma\Delta t\ddot{\mathbf{q}}_{k+1} \tag{46}$$

For a fixed rotational speed and time step, $\mathbf{S}_\mathrm{N}$ is LU-factorized in advance. The standard time-domain record uses

$$T = 3\ \mathrm{s},\ \Delta t = 5\times10^{-5}\ \mathrm{s},\ N = \frac{T}{\Delta t} + 1 = 60001 \tag{47}$$

2.6. Model Parameters and Validation

Table 1 summarizes the principal model, control, and numerical parameters.

The finite-element rotor model is validated against the free–free modal test of the same rotor reported in [16]. Figure 2 shows the first three bending mode shapes, and Table 2 compares the computed and measured natural frequencies. The maximum relative error is 1.361% (second bending mode), so the model reproduces the flexible dynamic characteristics of the test rotor and is used as the baseline model for the platform-motion analysis.

Table 2. Comparison of computed and measured free–free bending natural frequencies [16].

Mode	FE (Hz)	Exp. (Hz)	Error (%)
1st bending	127.04	127.0	0.031
2nd bending	283.39	287.3	1.361
3rd bending	643.53	642.4	0.176

Figure 3 shows the closed-loop Campbell diagram, obtained from the eigenvalues of Equation (36), and the steady unbalance response. The 1× line crosses the first two forward modes at $n_{c1} \approx 2990$ rpm ($\zeta = 0.054$) and $n_{c2} \approx 7600$ rpm ($\zeta = 0.33$). Shaft bending contributes about 45% of the first mode shape, so the rotor is flexible, and the scanned range 1000–7000 rpm passes through n_{c1}. The unbalance orbit varies non-monotonically with speed, peaking near 3000 rpm; it exceeds the ISO A/B limit (75 μm) between 2850 and 3200 rpm and stays below it at all scanned speeds. The unbalance (1.25×10^{-4} kg·m) represents the residual unbalance after balancing; its effect on the clearance zone is given by Equation (65).

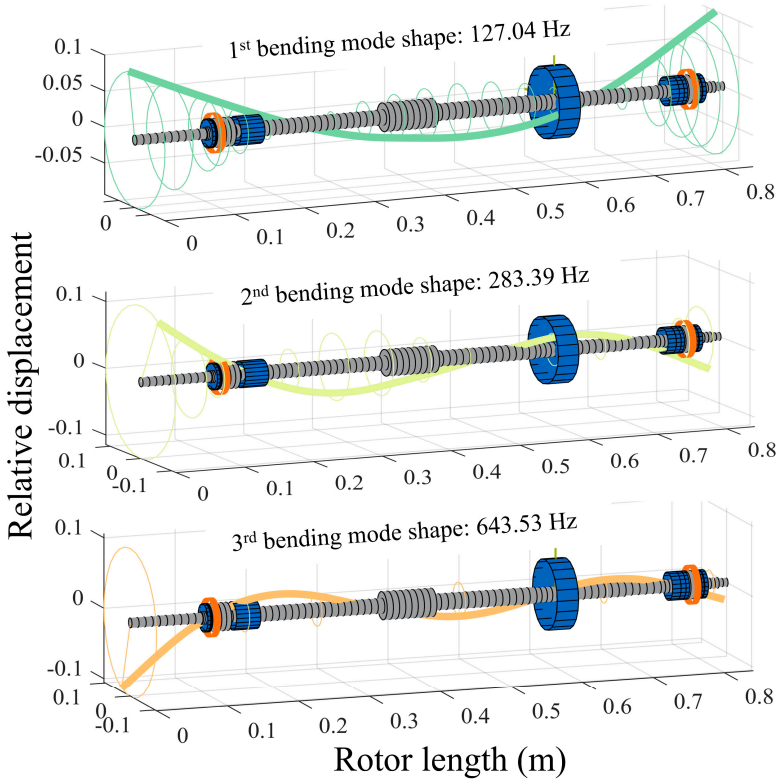


Figure 2. First three free–free bending mode shapes of the finite-element rotor model.

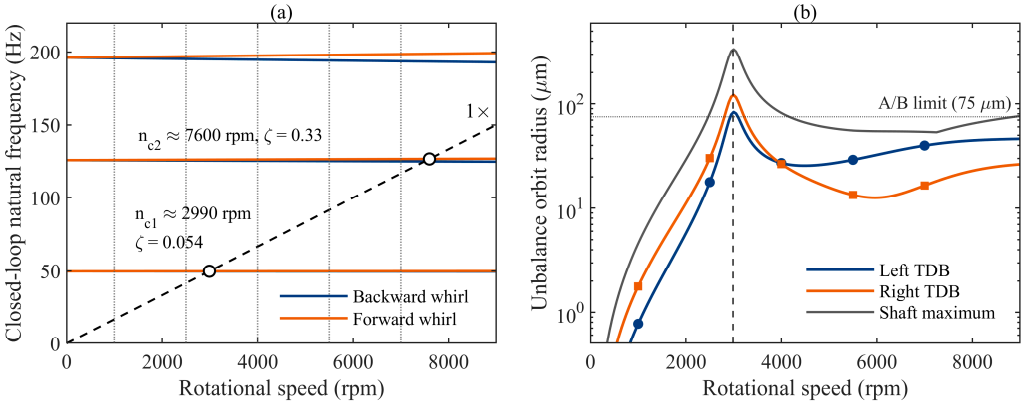


Figure 3. Closed-loop rotor dynamic characteristics: (**a**) Campbell diagram with the synchronous (1×) line and the five scanned speeds (dotted); (**b**) steady unbalance orbit radius at the left and right TDBs and the shaft maximum versus rotational speed.

3. Data Processing, Evaluation Metrics, and Parameter Scan

3.1. Time-Domain Data Extraction and Event Alignment

For each simulated case, complete time histories are stored at 36 prescribed axial positions, including $u_x(z_i, t_j)$, $u_y(z_i, t_j)$, and radial displacement. The three key sections, left, disk, and right, are all included among these sampling positions. The radial displacement is defined as

$$r(z_i, t_j) = \sqrt{u_x^2(z_i, t_j) + u_y^2(z_i, t_j)} \tag{48}$$

Full-record statistics are calculated from 60,001 time samples. The full-record radial peaks at the left and right supports are denoted by $r_{\mathrm{L,max}}$ and $r_{\mathrm{R,max}}$, respectively, and the larger value identifies the dominant support. The dominant direction is determined by comparing the full-record peaks of $|u_x|$ and $|u_y|$ at that support position.

The support-peak event is defined as

$$t_{\text{support}} = *argmax_t[\max(r_{\text{L}}(t), r_{\text{R}}(t))] \tag{49}$$

The local time coordinate is $\tau = t - t_{\text{support}}$, and the analysis window is $[-0.10, 0.30]$ s. At $\tau = 0$, the instantaneous u_x, u_y, and r values are extracted at all 36 axial positions to compare the axial shapes at the support-peak event.

3.2. Axial Response and Spatial-Distribution Metrics

The full-record maximum envelope and RMS envelope at each axial position are defined as

$$r_{\max}(z_i) = \max_j r(z_i, t_j),\ r_{\text{RMS}}(z_i) = \sqrt{\frac{1}{N}\sum_{j=1}^{N} r^2(z_i, t_j)} \tag{50}$$

The axial trajectory analysis uses the (u_x, u_y) samples within the selected time window. A two-dimensional sample covariance matrix is constructed at each axial position. Its eigenvectors give the principal component analysis (PCA) directions of the trajectory, and its eigenvalues give the trajectory scales along the two principal axes. The original trajectories at the left, disk, and right sections are shown together with the PCA ellipses at the 36 axial positions.

To characterize the axial location at which the radial response is concentrated, the response center is defined using r^2 as the weight:

$$z_c(t) = \frac{\sum_{i=1}^{N_z} z_i r^2(z_i, t)}{\sum_{i=1}^{N_z} r^2(z_i, t)} \tag{51}$$

where $N_z = 36$. The axial spatial width relative to the response center is defined as

$$\sigma_z(t) = \sqrt{\frac{\sum_{i=1}^{N_z} [z_i - z_c(t)]^2 r^2(z_i, t)}{\sum_{i=1}^{N_z} r^2(z_i, t)}} \tag{52}$$

z_c represents the axial location of the principal response region, whereas σ_z describes the axial extent of the response. The spatiotemporal response map is normalized by the maximum radial response within the local window for the corresponding case. The normalized axial shape at the support-peak event is scaled by the maximum radial response among the 36 sampling positions at that instant.

3.3. Key Response, Control Demand, and Spectral Descriptors

The internal flexible response at the disk section is represented by the maximum full-record radial displacement

$$r_{\text{D,max}} = \max_t \sqrt{u_x^2(z_{\text{D}}, t) + u_y^2(z_{\text{D}}, t)} \tag{53}$$

The radial magnitudes of the left and right AMB control forces are denoted by $F_j(t)$, and the maximum control demand is defined as

$$F_j(t) = \left\|\mathbf{f}_j(t)\right\|_2,\ j \in \{\text{L}, \text{R}\},\ F_{\text{AMB,max}} = \max_t[\max(F_{\text{L}}(t), F_{\text{R}}(t))] \tag{54}$$

The magnitude of the platform-equivalent load is represented by the temporal RMS of the two-norm of the global load vector:

$$F_{\text{base,RMS}} = \sqrt{\frac{1}{N}\sum_{j=1}^{N}\left\|\mathbf{F}_{\text{base}}(t_j)\right\|_2^2} \tag{55}$$

The signed $u_x(t)$ at the disk section is used for frequency-domain analysis. For spectral analysis, the simulations are extended to 12 s. After removal of the mean from the 6 s steady-state record ($3 \leq$ t $<$ 9 s), a rectangular-window one-sided FFT is calculated [49,50]. The rotational frequency is $f_r = n/60$, the platform frequency is denoted by f_b, and the target sideband frequencies are $f_- = f_r - f_b$ and $f_+ = f_r + f_b$. The spectral amplitude ratio at the target sideband frequencies is defined as

$$R_{\text{SB}} = \frac{A(f_r - f_b) + A(f_r + f_b)}{A(f_r)} \tag{56}$$

The target frequencies coincide with FFT frequency bins, at which $A(f)$ is evaluated directly.

3.4. TDB Clearance and Parameter-Path Metrics

The left and right TDBs are co-located with the corresponding AMB support sections, and the minimum TDB radial clearance is $C_{\text{min}} = 250$ μm. The instantaneous maximum support radial response, instantaneous clearance ratio, and full-record clearance ratio are defined, respectively, as

$$r_{\text{TDB}}(t) = \max[r_{\text{L}}(t), r_{\text{R}}(t)],\ \lambda_t(t) = \frac{r_{\text{TDB}}(t)}{C_{\text{min}}},\ \lambda_D = \max_t \lambda_t(t) \tag{57}$$

ISO 14839-2 [51] evaluates the shaft vibration of AMB-supported rotating machinery by the ratio of the displacement to the minimum TDB clearance, with zone limits of 0.3, 0.4, and 0.5 C_{min}: $\lambda_D < 0.3$ (zone A, newly commissioned machines), $0.3 \leq \lambda_D < 0.4$ (zone B, unrestricted long-term operation), $0.4 \leq \lambda_D < 0.5$ (zone C, operation for a limited period), and $\lambda_D \geq 0.5$ (zone D, vibration severe enough to cause damage). Zone D is used here as the risk threshold and zone C as a warning band. Because the model contains no rotor–TDB contact law, λ_D is a pre-contact clearance-margin indicator.

A sequence of samples that continuously satisfies $\lambda_t(t_j) \geq 0.5$ within the local time window is counted as one zone-D interval. The number of intervals is determined by counting contiguous sequences, and the cumulative duration is calculated using the corresponding sampling time step.

The parameter space consists of four platform degrees of freedom, five rotational speeds, and four amplitude and frequency multipliers: DOF $\in \{\text{heave}, \text{sway}, \text{pitch}, \text{yaw}\}$, $n \in \{1000, 2500, 4000, 5500, 7000\}$ rpm, and $a_s, f_s \in \{1, 2, 3, 4\}$. This gives a total of $4 \times 5 \times 4 \times 4 = 320$ discrete cases.

In addition to the complete 4×4 scan, two conditional paths, a1/f4→a4/f4 and a4/f1→a4/f4, are used. For any response metric Y, the endpoint amplification factors along the two paths are defined as

$$G_A(Y) = \frac{Y(\text{a4/f4})}{Y(\text{a1/f4})},\ G_F(Y) = \frac{Y(\text{a4/f4})}{Y(\text{a4/f1})} \tag{58}$$

Here, Y is taken as λ_D, the disk peak, or the maximum AMB control force. Within each representative slice, the ISO zone boundaries are first estimated from the 4×4 discrete

samples: when adjacent samples lie on opposite sides of a zone limit, linear interpolation between the two points determines the intersection, and the intersections form a boundary line in the parameter plane. These interpolated boundaries are verified against the closed-form boundaries derived in Section 3.6.

3.5. Statistical Analysis and Post-Processing Consistency Verification

The full-parameter statistics are based on 320 discrete cases. When grouped by platform degree of freedom or rotational speed, the median and maximum are used to describe the within-group distribution and upper bound. Linear associations between variables are measured using the Pearson correlation coefficient [52]

$$r_{XY} = \frac{\sum_{k=1}^{N_c} (X_k - \overline{X})(Y_k - \overline{Y})}{\sqrt{\sum_{k=1}^{N_c} (X_k - \overline{X})^2} \sqrt{\sum_{k=1}^{N_c} (Y_k - \overline{Y})^2}}, \; N_c = 320 \tag{59}$$

The correlation analysis includes the disk peak versus λ_D and base-force RMS versus the disk peak. It also includes the disk peak versus the maximum AMB control force, base-force RMS versus the maximum AMB control force, and the maximum AMB control force versus λ_D.

All simulations and post-processing are completed in the MATLAB R2024b environment. For the original 320-case scan, time-domain data are stored at 36 axial positions and 60,001 time samples per case. Key displacement peaks are independently recalculated from the original time histories and compared with the summary metric table, with an allowable difference of 10^{-4} μm. The spectral ratios are independently recalculated from the steady-state records. ISO zone classification, zone-D interval counts, grouped statistics, correlation coefficients, and extremum cases are all calculated from the discrete simulation samples.

3.6. Closed-Form TDB Envelope and ISO Zone Boundaries

The parameter scan of Section 3.4 resolves the zone boundaries at the 4×4 grid points. Because the rotor–AMB model is linear and the platform frequencies are far below the closed-loop natural frequencies, the boundaries can also be written in closed form. Only the lateral degrees of freedom are retained, and the response is split into the unbalance-forced part at Ω and the platform-forced part at ω_b:

$$\begin{aligned} &\mathbf{q}(t) = \mathbf{q}_{\mathrm{ub}}(t) + \mathbf{q}_b(t), \\ &\mathbf{Z}(\omega) = \mathbf{K} + \mathbf{K}_{x,\mathrm{comp}} - \omega^2\mathbf{M} + \mathrm{i}\omega(\mathbf{C} + \Omega\mathbf{G}) + k_i\left(K_P + \tfrac{K_I}{\mathrm{i}\omega} + \mathrm{i}\omega K_D\right)\sum_c \mathbf{L}_c^{\mathrm{T}}\mathbf{L}_c \end{aligned} \tag{60}$$

where $\mathbf{Z}(\omega)$ is the closed-loop dynamic stiffness obtained by substituting harmonic motion into Equations (36) and (37), and $\mathbf{L}_c$ is the localization vector of the c-th controlled AMB direction. The steady unbalance response is $\mathbf{Q}_{\mathrm{ub}} = \mathbf{Z}(\Omega)^{-1}\hat{\mathbf{F}}_{\mathrm{ub}}$, with $\hat{\mathbf{F}}_{\mathrm{ub}}$ the complex amplitude of Equation (15). Its orbit radius at the j-th TDB section ($j = L, R$) is

$$r_{\mathrm{ub},j}(\Omega) = \max_{\varphi\in[0,2\pi)} \left| \mathrm{Re}\left(X_j e^{\mathrm{i}\varphi}\right) + \mathrm{iRe}\left(Y_j e^{\mathrm{i}\varphi}\right) \right| \tag{61}$$

where X_j and Y_j are the x and y entries of $\mathbf{Q}_{\mathrm{ub}}$ at the TDB node. The platform load of Equation (24) is harmonic at ω_b. For translation along x (heave in the present labeling; sway is identical along y) and for the rotation that produces x-displacement (pitch; yaw is identical along y), the peak platform-induced displacement at the TDB is

$$b_j = A_b\omega_b^2 h_j \text{ (translation)}, \; b_j = \Theta_b\omega_b^2 e_j - g\sin\Theta_b h_j \text{ (rotation)} \tag{62}$$

where $h_j = \left|\mathbf{e}_j^{\mathrm{T}}\mathbf{Z}(\omega_b)^{-1}\mathbf{m}\right|$ and $e_j = \left|\mathbf{e}_j^{\mathrm{T}}\mathbf{Z}(\omega_b)^{-1}\mathbf{m}_z\right|$ are the TDB compliances to a unit translational and a unit angular platform acceleration, $\mathbf{m}$ collects the nodal masses of Equation (23), $\mathbf{m}_z$ collects the products $m_i z_i$, and the second term of the rotational case is the gravity projection in Equation (22). Since $\Omega/\omega_b \geq 8$ for all cases, the unbalance orbit completes many revolutions within one platform period, so the orbit passes the direction of the platform offset near its peak. The peak TDB displacement is therefore

$$D_{\max} \approx \max_{j=L,R}\left[r_{\mathrm{ub},j}(\Omega) + |b_j|\right],\ \lambda_D = \frac{D_{\max}}{C_{\min}} \tag{63}$$

The closed-loop dynamic stiffness simplifies at the platform frequencies. The integral corner frequency $K_I/K_P = 1.7 \times 10^{-3}$ rad/s is far below ω_b, and the lowest closed-loop natural frequency (49.2 Hz) is more than 24 times the highest platform frequency (2 Hz). Hence $\mathbf{Z}(\omega_b) \approx \mathbf{K} + k_i K_P \sum_c \mathbf{L}_c^{\mathrm{T}}\mathbf{L}_c$ and the compliances are quasi-static: between 0.5 and 2 Hz, h_j varies by less than 0.15% and is independent of Ω (the gyroscopic term is multiplied by ω_b). The finite-element values are $h_L = 1.78$ and $h_R = 1.51$ µm per m/s^2. For heave and sway, substituting $A_b = a_s A_{b,0}$ and $\omega_b = f_s \omega_{b,0}$ into Equations (62) and (63) and setting $D_{\max} = \lambda C_{\min}$ gives the zone boundary explicitly:

$$a_s f_s^2 = \Pi_\lambda(\Omega) = \min_{j=L,R} \frac{\lambda C_{\min} - r_{\mathrm{ub},j}(\Omega)}{A_{b,0}\omega_{b,0}^2 h_j},\ \lambda \in \{0.3, 0.4, 0.5\} \tag{64}$$

Equation (64) shows that the ISO boundaries in the (a_s, f_s) plane are hyperbolae $a_s = \Pi_\lambda / f_s^2$, i.e., the zone is governed by the platform acceleration amplitude $a_b = A_b\omega_b^2$ the product of amplitude and squared frequency. The rotational speed enters only through the unbalance orbit, which lowers the boundary by $r_{\mathrm{ub},j}/(A_{b,0}\omega_{b,0}^2 h_j)$. The equivalent critical acceleration is

$$a_{b,\lambda}^*(\Omega) = \min_{j=L,R} \frac{\lambda C_{\min} - r_{\mathrm{ub},j}(\Omega)}{h_j} \tag{65}$$

For pitch and yaw, the Euler term $\Theta_b\omega_b^2 e_j$ and the gravity projection $g \sin\Theta_b h_j$ have opposite signs. With $e_L = 0.53$ and $e_R = 0.87$ µm per rad/s^2, the two terms nearly cancel at the left TDB when $\omega_b^2 \approx g h_L / e_L$ (about 0.9 Hz), which explains why the pitch and yaw responses at $f_s \leq 2$ stay close to the unbalance level. At $f_s \geq 3$ the Euler term dominates and the boundary again approaches a hyperbola; it is obtained from Equations (62) and (63) numerically.

Equations (60)–(63) require only one complex linear solve per frequency and no time integration. Table 3 lists the resulting coefficients. Compared with the steady-state part ($t \geq 1$ s) of the 320 time-domain simulations, the closed-form envelope gives a coefficient of determination of 0.997, a maximum error of 0.014 $C_{\min}$ and a root-mean-square error of 0.006 $C_{\min}$. It assigns the same ISO zone as the simulation in 316 of the 320 cases; the remaining four lie within 0.015 $C_{\min}$ of a zone limit. The full-record $D_{\max}$ additionally contains the start-up transient from the zero initial state, which sets a floor of 0.17–0.24 $C_{\min}$ at 2500–7000 rpm, below the A/B limit. For all cases with $D_{\max} \geq 0.3C_{\min}$, the full-record value and the closed form differ by at most 0.026 $C_{\min}$.

Table 3 quantifies the margin between the scanned excitation and the zone limits. Entering zone D under heave or sway requires a platform acceleration of 4.9 g at 7000 rpm and 7.1 g at 1000 rpm, and the corresponding value of $a_s f_s^2$ (48.5–70.8) is reached only near the a4/f4 corner of the scan ($a_s f_s^2 = 64$). The decrease of $a_{b,\lambda}^*$ with rotational speed is caused entirely by the growth of the left unbalance orbit from 0.8 to 39.8 µm, which consumes up to 32% of the 0.5 $C_{\min}$ budget at 7000 rpm. Because the platform compliance is speed-independent, Equation (65) also gives the zone for any other harmonic sea-state

component: a measured or specified platform acceleration amplitude can be compared directly with $a^*_{b,\lambda}(\Omega)$ without repeating the time-domain scan.

Table 3. Steady-state unbalance orbit radii and approximate ISO 14839-2 zone-boundary thresholds at different rotational speeds.

Speed (rpm)	$r_{ub,L}$ (μm)	$r_{ub,R}$ (μm)	$a^*_{b,0.3}$ (g)	$a^*_{b,0.4}$ (g)	$a^*_{b,0.5}$ (g)	$\Pi_{0.5}=a_s f_s^2$
1000	0.8	1.8	4.25	5.69	7.12	70.8
2500	17.7	30.2	3.03	4.72	6.15	61.1
4000	27.1	26.5	2.75	4.18	5.61	55.8
5500	29.1	13.3	2.63	4.07	5.50	54.7
7000	39.8	16.5	2.02	3.45	4.88	48.5

4. Results and Discussion

4.1. Stronger Platform Excitation Changes Rotor Responses at Key Positions

Under heave at 4000 rpm, Figure 4 compares three combined excitation states: a1/f1, a3/f4, and a4/f4. In Figure 4a, the dominant-support peaks are 52.14, 111.61, and 139.73 μm, respectively, and the disk peaks are 141.8, 264.4, and 325.3 μm. The corresponding disk-to-dominant-support peak ratios are approximately 2.72, 2.37, and 2.33. The dominant support changes from right at a1/f1 to left at a3/f4 and a4/f4.

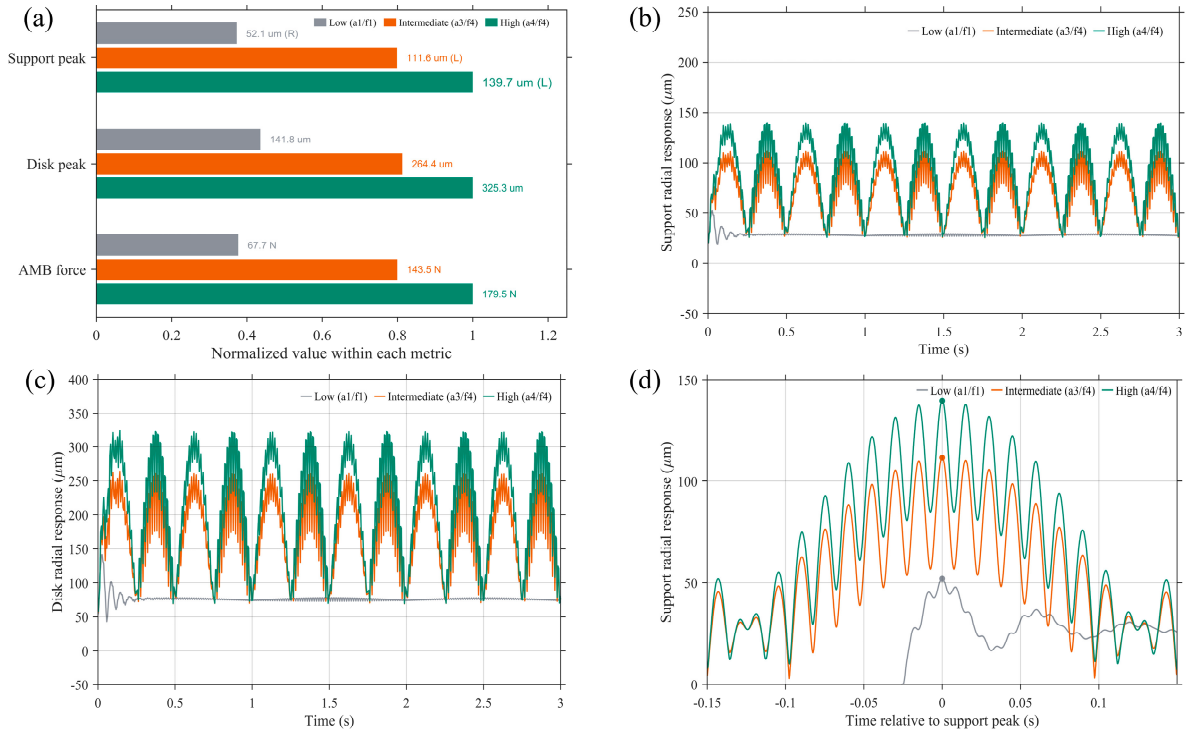


Figure 4. At 4000 rpm under heave, comparison of key responses for three combined excitation states (a1/f1, a3/f4, and a4/f4): (**a**) dominant-support peak, disk peak, and maximum AMB control force; (**b**) complete time history of the dominant-support radial response; (**c**) complete time history of the disk radial response; and (**d**) local support response with the support-peak event set to time zero.

According to Equations (19) and (24), higher amplitude and frequency levels increase the platform-equivalent inertial load, which is transmitted through the AMB supports and excites the bending response of the shaft between them. Because the lowest closed-loop natural frequency (49.2 Hz) lies far above the platform frequencies (at most 2 Hz), the platform-induced component of this response is quasi-static (Section 3.6): the shaft deflects

in the static shape of the closed-loop system under a distributed inertial load, which is largest in the span between the supports. The total response additionally contains the synchronous unbalance orbit and the start-up transient, and the disk peak exceeds the support peak by a factor of 2.3–2.7 in all three states. Under weak excitation, the support response is dominated by the unbalance orbit, which is of similar size at the two supports. Under strong excitation, the platform term dominates, and since $h_L > h_R$ the left support becomes dominant.

4.2. Platform Degrees of Freedom Affect Directionality and Axial Flexible Shapes

At 4000 rpm under a4/f4, Figure 5 compares the four platform degrees of freedom. Figure 5a,e shows that the heave response is dominated by the x direction, with a peak of 139.73 μm. Sway is dominated by the y direction, with a peak of 139.68 μm. The dominant directions for pitch and yaw are x and y, with peaks of 113.87 and 115.31 μm, respectively. In Figure 5b, the dominant support is left for heave and sway and right for pitch and yaw.

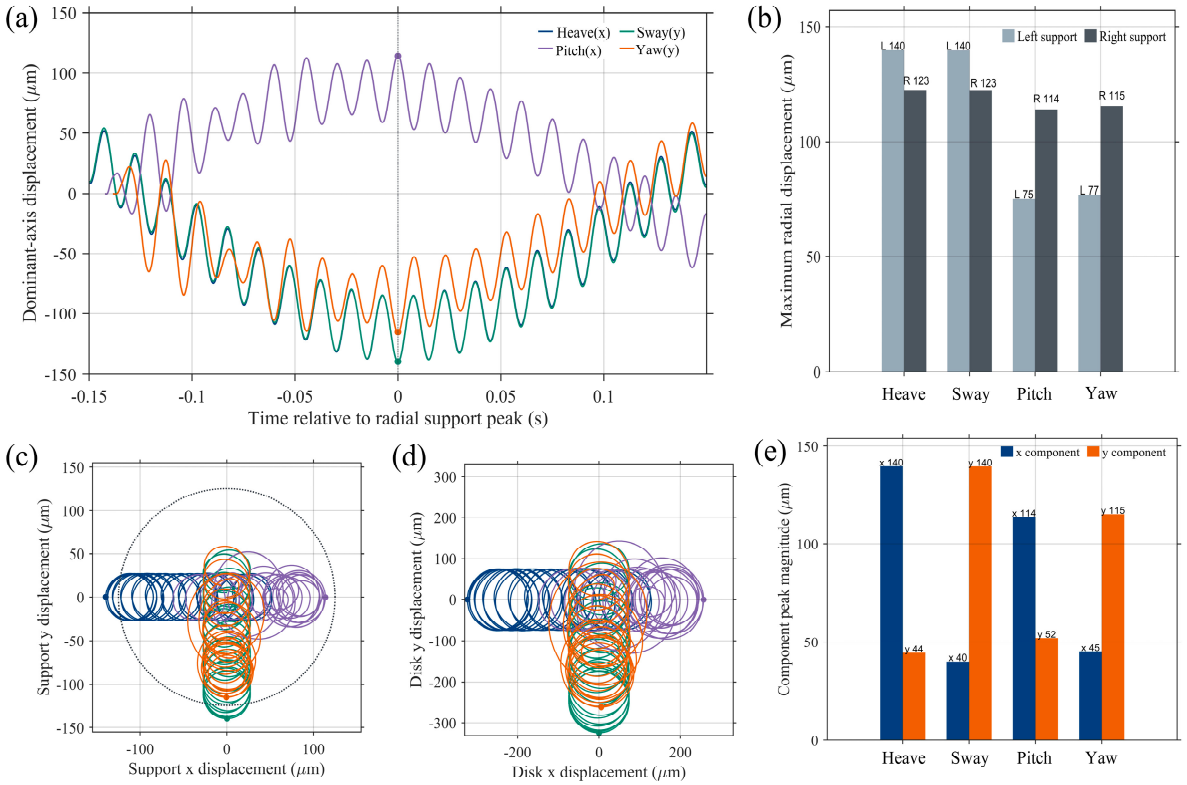


Figure 5. Directional responses for different platform degrees of freedom at 4000 rpm under a4/f4: (**a**) peak-aligned time histories of the dominant-direction displacement; (**b**) maximum radial displacements at the left/right supports; (**c**) dominant-support trajectory; (**d**) disk trajectory; and (**e**) peaks of the x and y components.

The directional differences follow from the load structure in Equation (22). Heave and sway produce transverse inertial loads that are nearly in phase along the shaft, whereas the Euler term $\dot{\vec{\omega}}_b \times \mathbf{r}_i$ for pitch and yaw varies with the axial position of the node and gives a non-uniform distributed load. The two load distributions excite the flexible modes differently, which changes the dominant direction, the hotspot position, and the left–right support relationship. The compliances of Section 3.6 quantify the support relationship: a unit translational acceleration gives $h_L = 1.78$ and $h_R = 1.51$ μm per m/s^2, whereas a unit angular acceleration gives $e_L = 0.53$ and $e_R = 0.87$ μm per rad/s^2. Translation therefore loads the left support more, and rotation loads the right support more. The peaks under

pitch and yaw are smaller because the gravity projection in Equation (22) partly offsets the Euler term.

Figure 6a–c shows the principal-direction ellipses of the trajectories at the 36 axial sampling positions within the selected time window, with the trajectories at the left AMB, disk, and right AMB superimposed. From a1/f1 through a3/f4 to a4/f4, the trajectories grow at most axial positions, and the principal direction changes along the shaft.

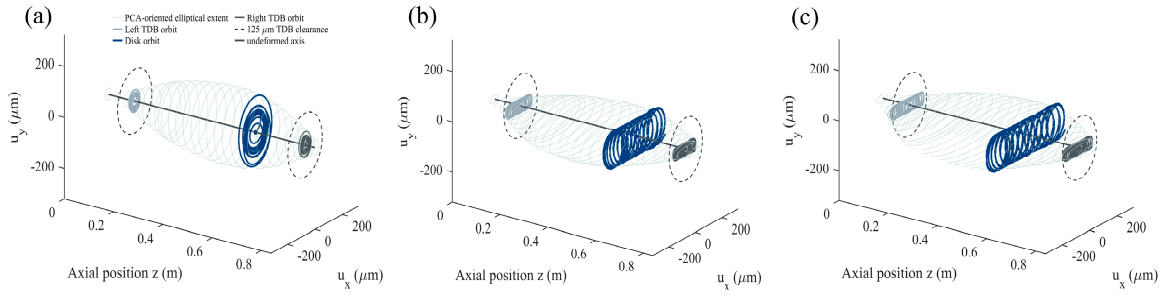


Figure 6. At 4000 rpm under heave, trajectory fields at 36 axial sampling positions and trajectories at key sections: (**a**) a1/f1; (**b**) a3/f4; and (**c**) a4/f4. Light-colored ellipses indicate the PCA principal directions and scales of the trajectories at the axial positions, and dashed circles indicate the TDB radial clearance.

Figure 7a shows the full-record axial maximum envelope. The maximum radial displacements over the complete shaft are 152.04, 291.19, and 358.49 μm for the three states, respectively. The peak position shifts from $z = 0.505$ m to $z = 0.473$ m. The maximum RMS values in Figure 7b are 82.10, 167.52, and 211.32 μm, respectively, all at $z = 0.473$ m. The RMS maximum stays at $z = 0.473$ m in all three states, whereas the instantaneous extremum moves between neighboring sections as the excitation level changes.

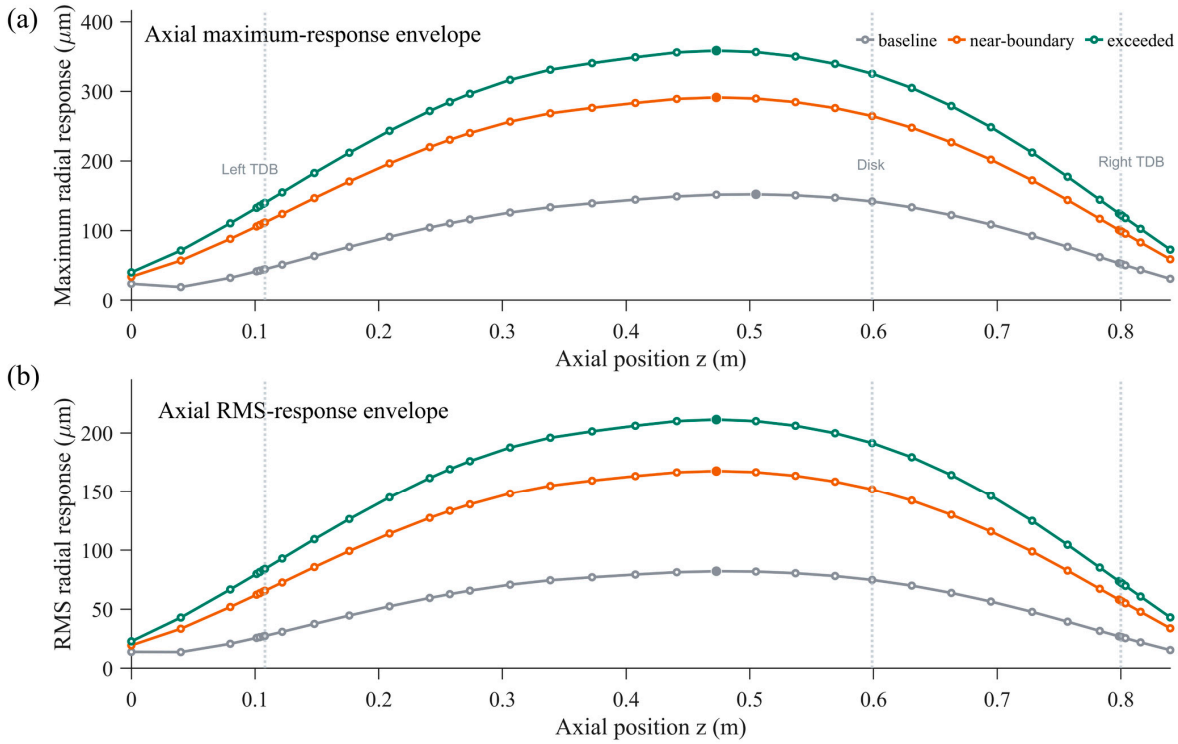


Figure 7. Axial radial-response envelopes for three combined excitation states under heave at 4000 rpm: (**a**) full-record maximum envelope and (**b**) RMS envelope. Vertical dashed lines mark the axial positions of the left TDB, disk, and right TDB.

Figure 8a,b shows the spatiotemporal variation in the axial response aligned with the support-peak event. According to the definitions in Equations (51) and (52), Figure 8c gives axial response centers for a1/f1, a3/f4, and a4/f4 of $z = 0.469$, 0.450, and 0.450 m, respectively. The spatial standard deviations in Figure 8d are 0.159, 0.165, and 0.166 m, respectively.

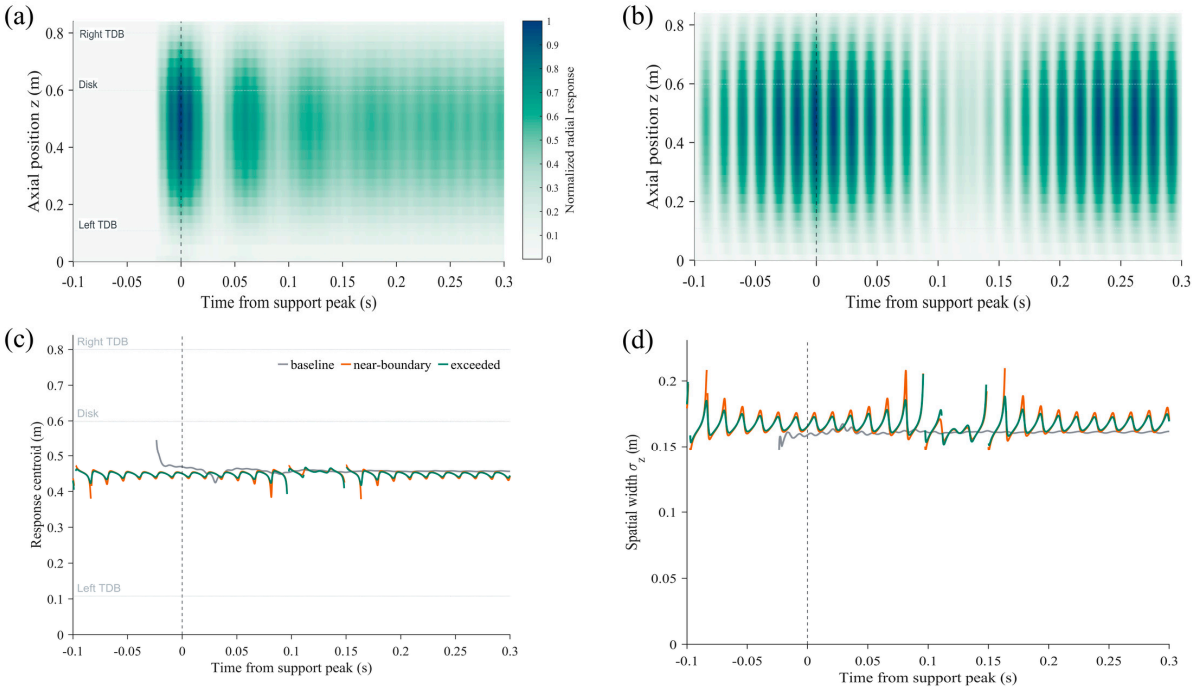


Figure 8. Axial spatiotemporal response and spatial statistics near the support-peak event: (**a**) normalized radial response in the a1/f1 case; (**b**) normalized radial response in the a4/f4 case; (**c**) response center z_c for the three states; and (**d**) spatial width σ_z.

Figure 9a–c extracts the instantaneous shapes at the same event time. The instantaneous full-shaft maxima for the three cases are 151.34, 284.62, and 353.20 µm, respectively, and the maximum position shifts from $z = 0.505$ m to $z = 0.473$ m. Figure 9d shows the corresponding normalized radial shapes.

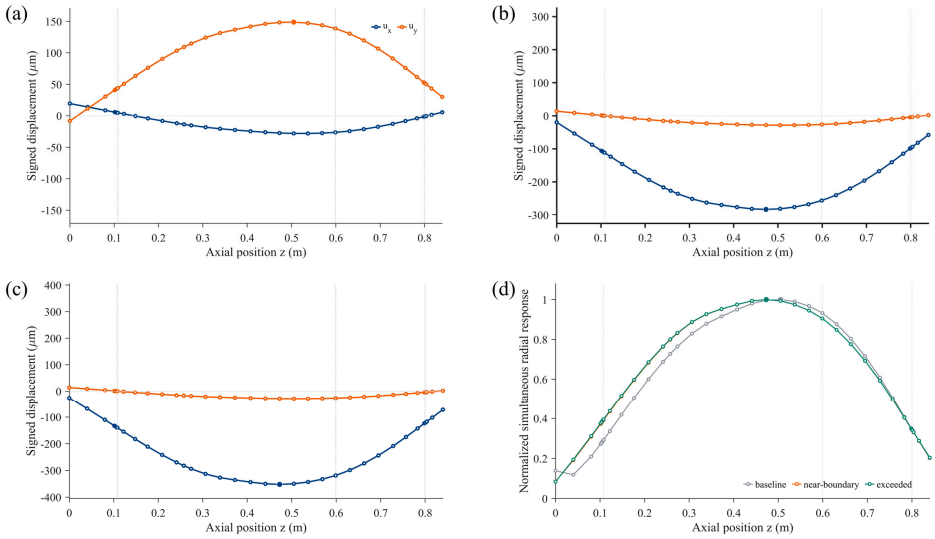


Figure 9. Instantaneous axial displacement shapes at the support-peak event: the u_x and u_y components under (**a**) a1/f1, (**b**) a3/f4, and (**c**) a4/f4; and (**d**) the normalized radial shapes for the three states.

Figures 6–9 show that, under stronger excitation, the peak amplitude grows and the hotspot moves, whereas the response center shifts only slightly to the left and the spatial standard deviation changes little. The axial extent of the response is therefore nearly unchanged. Because the platform-induced deflection is quasi-static, its axial shape is fixed by the closed-loop stiffness and only its amplitude scales with the excitation. The hotspot shift reflects the changing weight of this shape relative to the unbalance response, whose axial shape differs.

4.3. Support-Position Response and TDB Clearance Metric

The left and right TDBs are co-located with the corresponding AMB support sections, and λ_D characterizes the local clearance state. Figure 10a,b shows the support responses along the amplitude and frequency paths under heave at 4000 rpm. Figure 10c shows the corresponding λ_D calculated using Equation (57). With f4 fixed, the λ_D values from a1 to a4 are 0.229, 0.336, 0.446, and 0.559. With a4 fixed, the values from f1 to f4 are 0.209, 0.222, 0.366, and 0.559. Both paths reach their shared endpoint, a4/f4, which lies in zone D, but they grow differently. By Equation (62), the platform-induced part is proportional to a_s and to f_s^2: along the amplitude path λ_D rises by about 0.11 per level, whereas along the frequency path the f1 and f2 values stay near the level set by the unbalance orbit and the start-up transient, and the values rise steeply at f3 and f4. Inspection of the original samples in the local window from 1.80 to 2.20 s identifies 10 zone-D intervals ($\lambda_t \geq 0.5$) with a total duration of 0.04735 s.

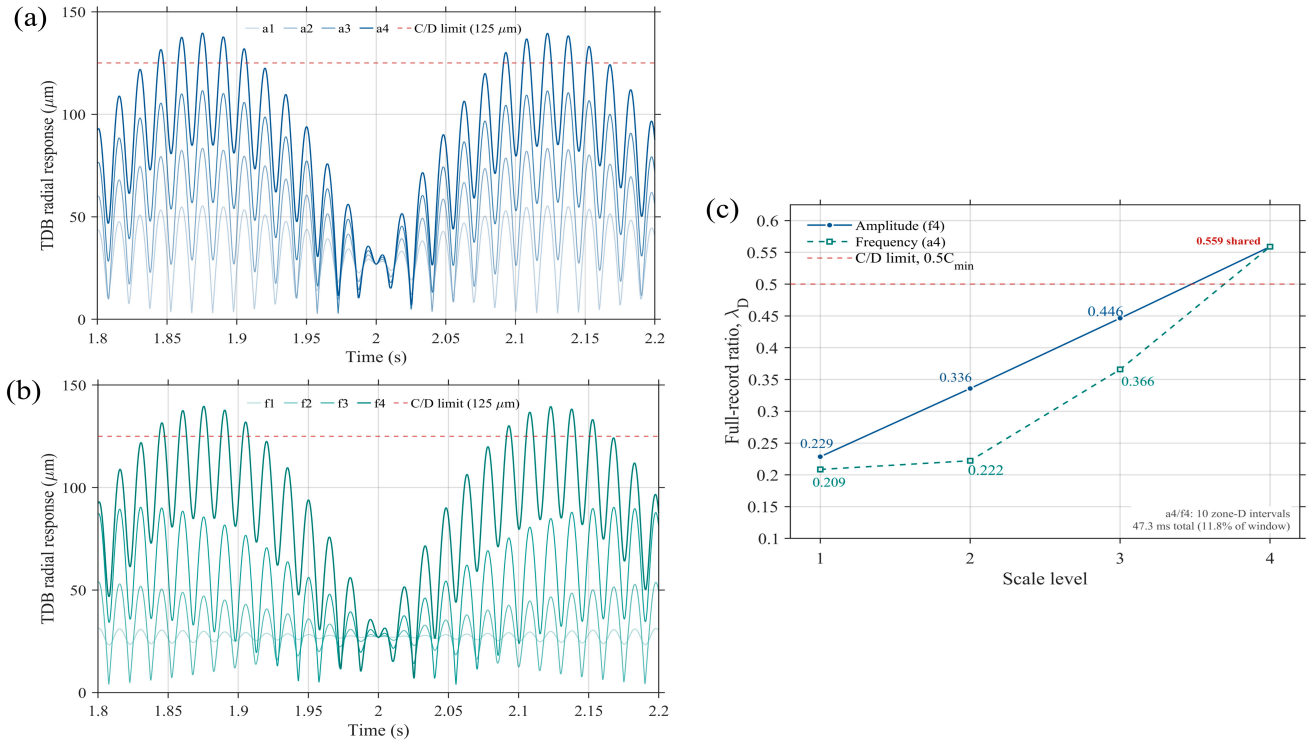


Figure 10. TDB support response and clearance ratio along the amplitude and frequency paths under heave at 4000 rpm: (**a**) with f4 fixed, radial response from a1 to a4; (**b**) with a4 fixed, radial response from f1 to f4; and (**c**) full-record λ_D along both paths. Dashed lines indicate the ISO 14839-2 C/D limit, $0.5C_{\text{min}} = 125$ μm.

4.4. Clearance Distribution, Rotational-Speed Effects, and Conditional Boundaries in the Full-Parameter Scan

Figure 11 summarizes 4 degrees of freedom, 5 rotational speeds, and 4 × 4 amplitude–frequency combinations, giving 320 discrete cases. Figure 11b shows that 256, 35, 19, and 10 cases fall in zones A, B, C, and D, respectively. The 10 zone-D cases are divided equally

between heave and sway, whereas all pitch and yaw samples remain below the C/D limit, with a maximum of 0.469. The critical side is left in every zone-D case, because the platform term dominates there and h_L exceeds h_R by 18%. In Figure 11c, the global maximum λ_D occurs at 7000 rpm under sway with a4/f4. Its value is 0.635, corresponding to a peak displacement of 158.63 µm at the TDB position. Figure 11a gives an overall Pearson correlation coefficient of 0.955 between the disk peak and λ_D; the scatter comes from the condition-dependent ratio between the disk bending response and the support displacement.

Figure 12a–d summarizes λ_D, the disk peak, the maximum AMB control force, and the steady-state spectral ratio for the 80 discrete cases in each platform degree of freedom. The maximum λ_D values for heave and sway are 0.627 and 0.635, respectively, and both groups contain zone-D samples. The maximum values for pitch and yaw are both 0.469 (zone C). The within-group maxima of the disk peak are 328.10, 328.15, 258.62, and 262.34 µm, respectively. The corresponding maximum AMB control forces are 203.71, 206.19, 150.17, and 150.19 N. The translational degrees of freedom give higher TDB, disk, and control-force values than the tilting ones, consistent with the directional results in Figure 5.

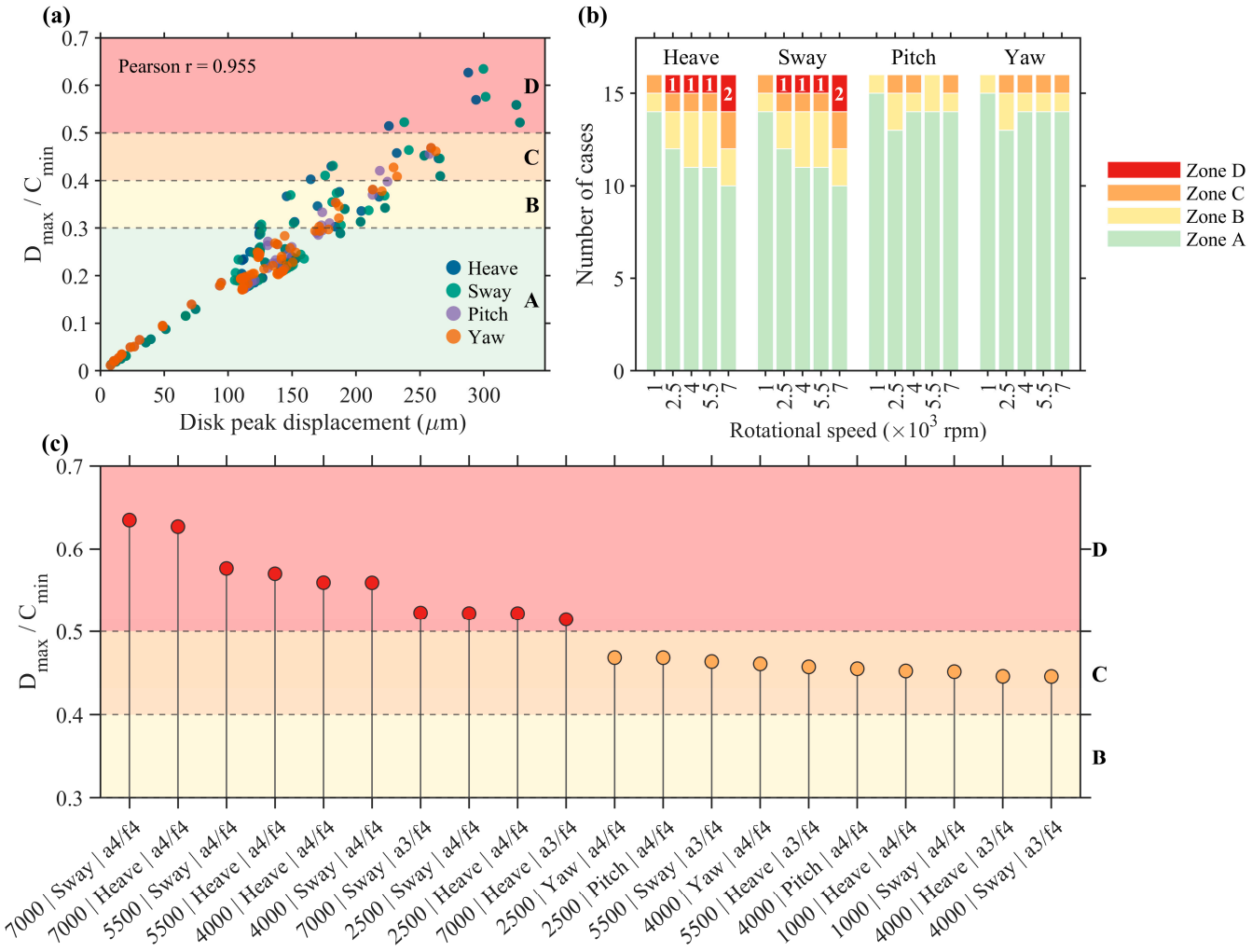


Figure 11. ISO 14839-2 zone statistics of the TDB clearance ratio for 320 discrete cases (C_{min} = 250 µm; zone limits 0.3, 0.4, and 0.5 C_{min}): (**a**) relationship between the disk peak and λ_D; (**b**) number of cases in each zone for each degree of freedom and rotational speed; and (**c**) the 20 highest-ratio cases ranked by λ_D.

Figure 13 shows that the extrema of different response metrics occur at different rotational speeds. The upper bounds of λ_D for heave and sway enter zone D from 2500 rpm

upwards and reach their maxima at 7000 rpm. Since the platform compliance varies by less than 0.15% with rotational speed (Section 3.6), the speed raises this upper bound through the unbalance orbit, which grows at the left TDB from 0.8 µm at 1000 rpm to 39.8 µm at 7000 rpm. The global maximum disk response is 328.15 µm and occurs at 2500 rpm under sway, the scanned speed closest to the first critical speed $n_{c1} \approx 2990$ rpm (Figure 3). The maximum AMB control force of 206.19 N occurs at 7000 rpm under sway with a4/f4. As shown by Equations (14) and (36), rotational speed changes the Ω^2 scale of the unbalance load, the gyroscopic term $\Omega\mathbf{G}$, and the closed-loop dynamic response, so these peaks occur at different speeds.

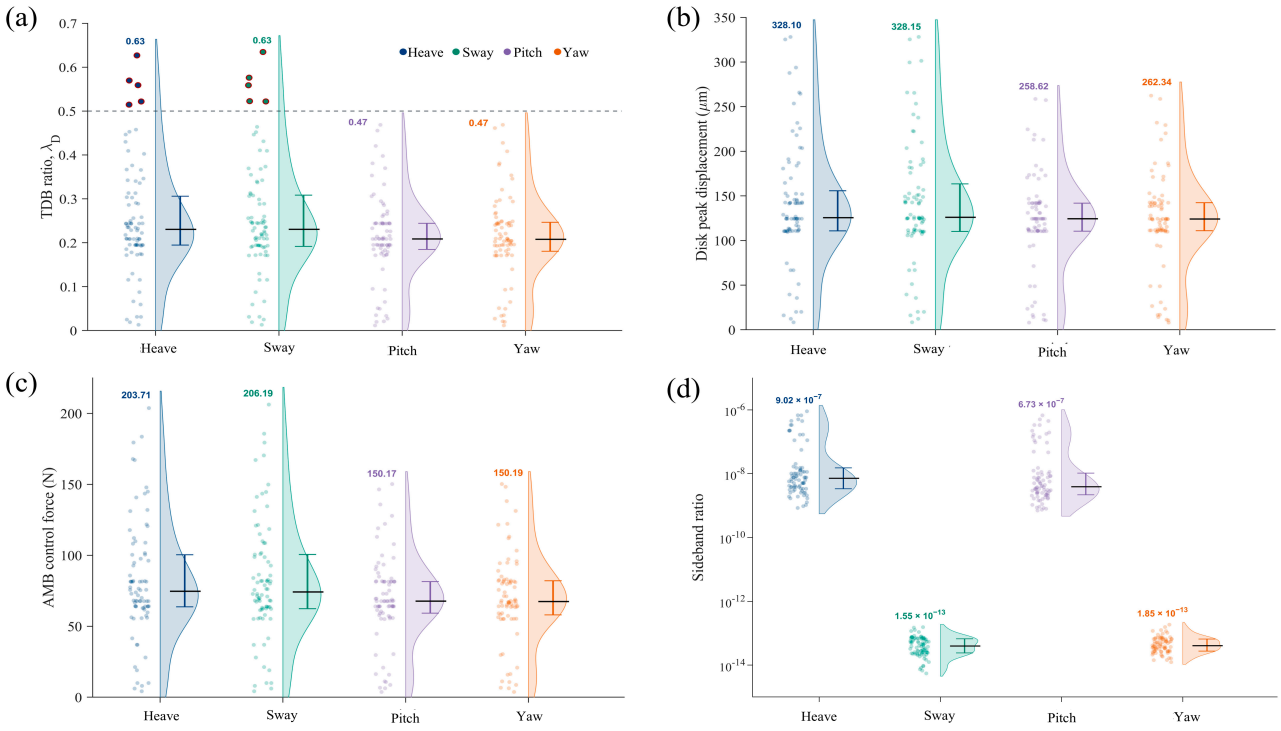


Figure 12. Metric distributions for the 80 cases under each of the four platform degrees of freedom: (**a**) TDB λ_D; (**b**) disk peak; (**c**) maximum AMB control force; and (**d**) steady-state spectral ratio from Equation (56). Labeled values are the maxima of the corresponding groups.

Figure 14a–d compares the two conditional paths, a1/f4 → a4/f4 and a4/f1 → a4/f4, for heave, sway, pitch, and yaw, respectively. The endpoint amplification factors are calculated using Equation (58). At the selected rotational speeds, the frequency-path endpoint amplification of λ_D and of the AMB control force exceeds that of the amplitude path. The disk response also shows greater amplification along the frequency path for sway, pitch, and yaw, whereas the two paths give similar factors for heave. According to Equation (19), the acceleration amplitude of the harmonic platform displacement is $A_b\omega_b^2$, so the frequency multiplier raises the equivalent inertial input in Equations (23) and (24) quadratically, whereas the amplitude multiplier raises it linearly. For pitch and yaw, the low-frequency end of the frequency path also lies near the cancelation of the Euler term and the gravity projection at about 0.9 Hz (Section 3.6), which keeps the starting value small and increases the amplification.

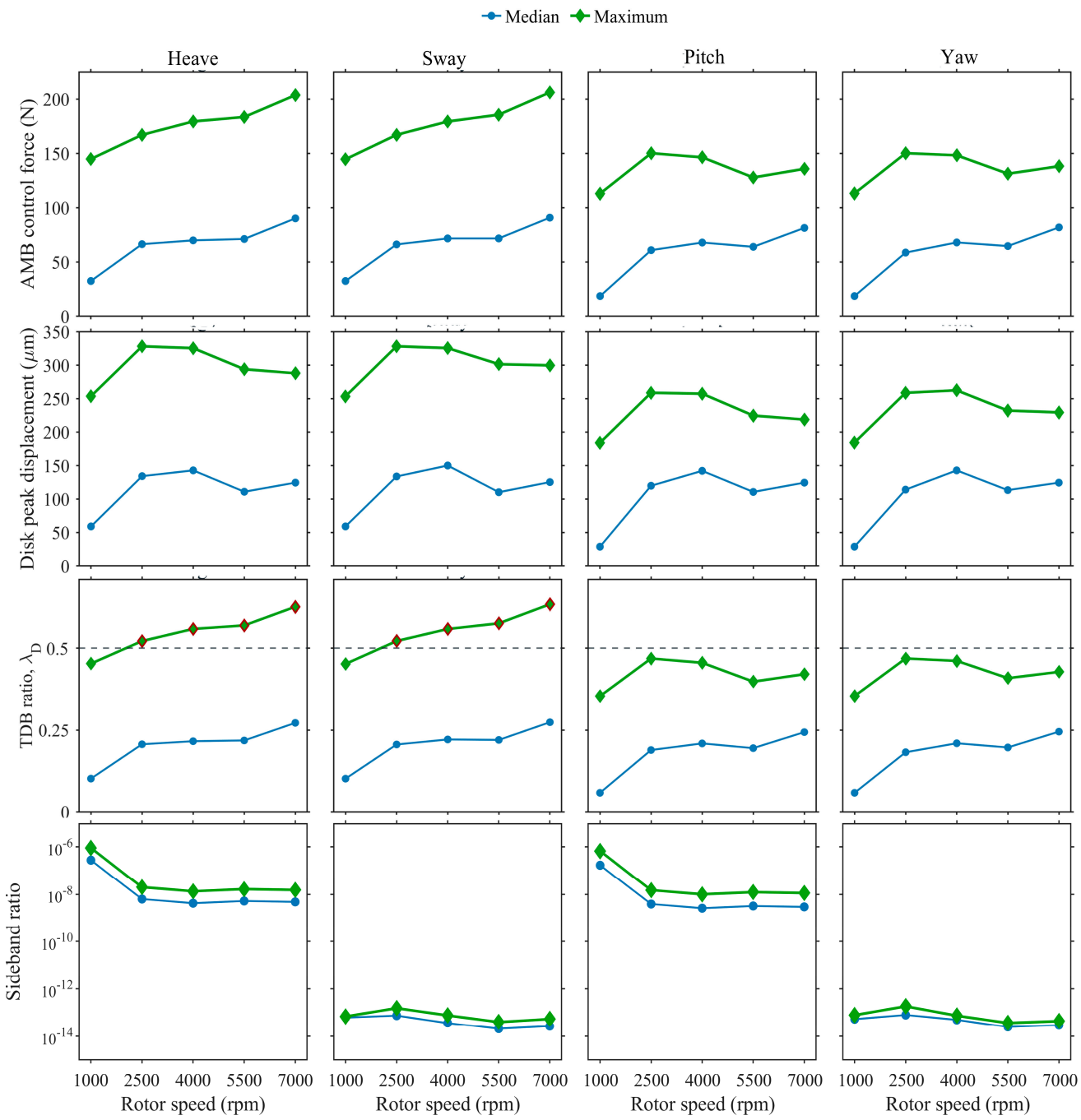


Figure 13. Response statistics for the four platform degrees of freedom at different rotational speeds. Columns correspond, from left to right, to heave, sway, pitch, and yaw. Rows correspond, from top to bottom, to the maximum AMB control force, disk peak, TDB λ_D, and steady-state spectral ratio. The blue and green lines represent the median and maximum, respectively.

Figure 15 shows the ISO zones of the 4×4 discrete samples in the representative slices on the amplitude–frequency plane. The filled contours and solid lines are interpolated from the samples, and the dashed lines are the closed-form boundaries of Equation (64). Figure 15a,b shows that, at 7000 rpm, 2 of the 16 cases are in zone D for both heave and sway. These are a3/f4 and a4/f4 in both cases, and the maximum λ_D values are 0.627 and 0.635, respectively. In Figure 15c,d, at 2500 rpm, no pitch or yaw sample reaches zone D, and the maximum λ_D is 0.469 in both cases (zone C at a4/f4). The zone-D points for heave and sway are concentrated at f4, consistent with the increase in the platform-acceleration scale caused by a higher frequency multiplier. The closed-form boundaries follow the hyperbolae

$a_s f_s^2 = \Pi_\lambda(\Omega)$ and pass through the same grid cells as the interpolated boundaries; between grid points the interpolated lines lie lower, because linear interpolation overestimates a response that grows with f_s^2.

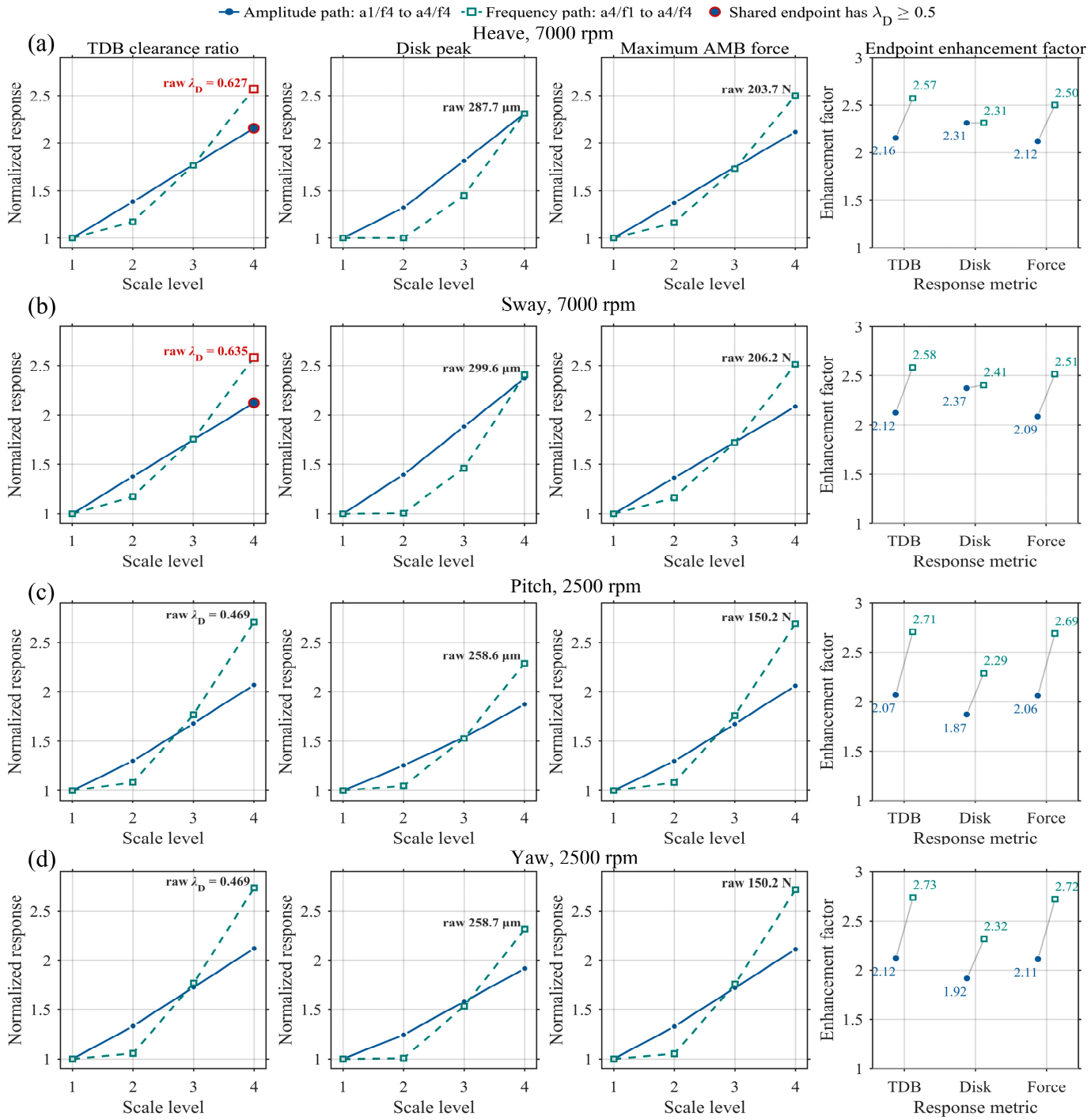


Figure 14. Conditional response comparison between the amplitude and frequency paths: (**a**) heave at 7000 rpm; (**b**) sway at 7000 rpm; (**c**) pitch at 2500 rpm; and (**d**) yaw at 2500 rpm. The first three columns show the normalized TDB λ_D, disk peak, and maximum AMB control force, respectively, and the fourth column gives the endpoint amplification factors along the two paths.

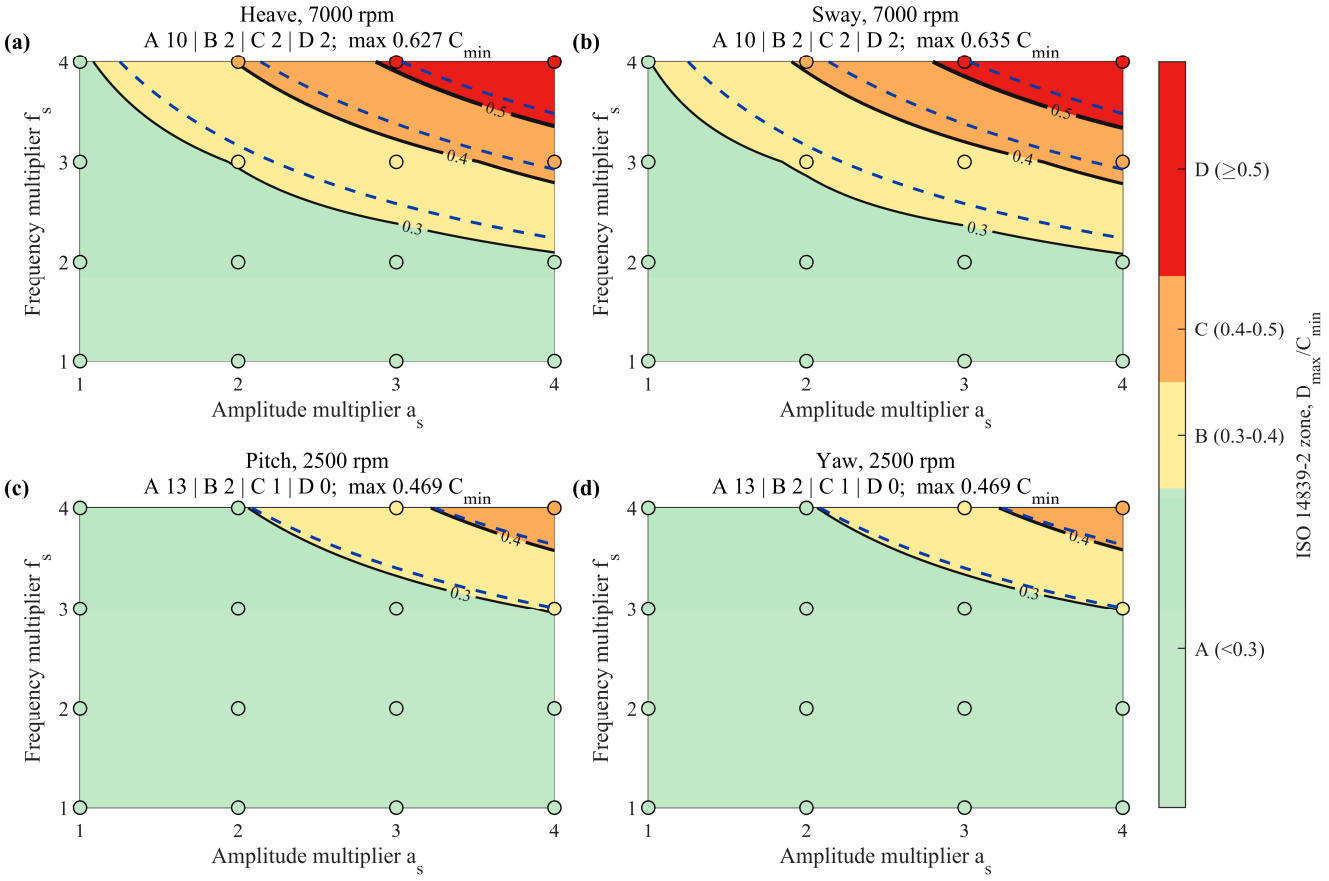


Figure 15. ISO 14839-2 zone boundaries of the TDB clearance ratio λ_D on the amplitude–frequency multiplier plane: (**a**) heave and (**b**) sway at 7000 rpm; (**c**) pitch and (**d**) yaw at 2500 rpm ($C_{\min} = 250$ µm). Filled contours and solid black lines are interpolated from the 4×4 time-domain cases; markers show the zone of each case. Dashed blue lines are the closed-form boundaries of Equations (62)–(64) at 0.3, 0.4, and 0.5 $C_{\min}$.

4.5. Spectral Observations and Load–Response–Control Relationships

Figure 16 presents the spectral results calculated from the 6 s steady-state interval. Panels (a, c) show the variation in the spectral ratio with excitation level, panel (b) shows the local spectrum around the rotational frequency, and panel (d) compares the same x-direction component across platform motions. Over all 320 cases, the ratio is at most 9.0×10^{-7} (Figures 12d and 13): the steady-state disk response consists of the synchronous and platform-frequency components, as Equation (60) predicts for the linear model.

Figure 17a–d uses the same 320 discrete cases. Equation (59) gives the Pearson correlations of base-force RMS with the disk peak and of the disk peak with the maximum AMB control force. It also gives the correlations of base-force RMS with the maximum AMB control force and of the maximum AMB control force with λ_D. The corresponding r values are 0.772, 0.949, 0.797, and 0.9995, respectively. The maximum AMB control force has the highest correlation with λ_D because both are set by the same support displacement: at the platform frequencies the integral and derivative actions are negligible (Section 3.6), so the control force follows the support displacement linearly. The disk peak additionally contains the shaft bending between the supports, and the base-force RMS is a record-averaged input rather than a peak, so both correlate less closely.

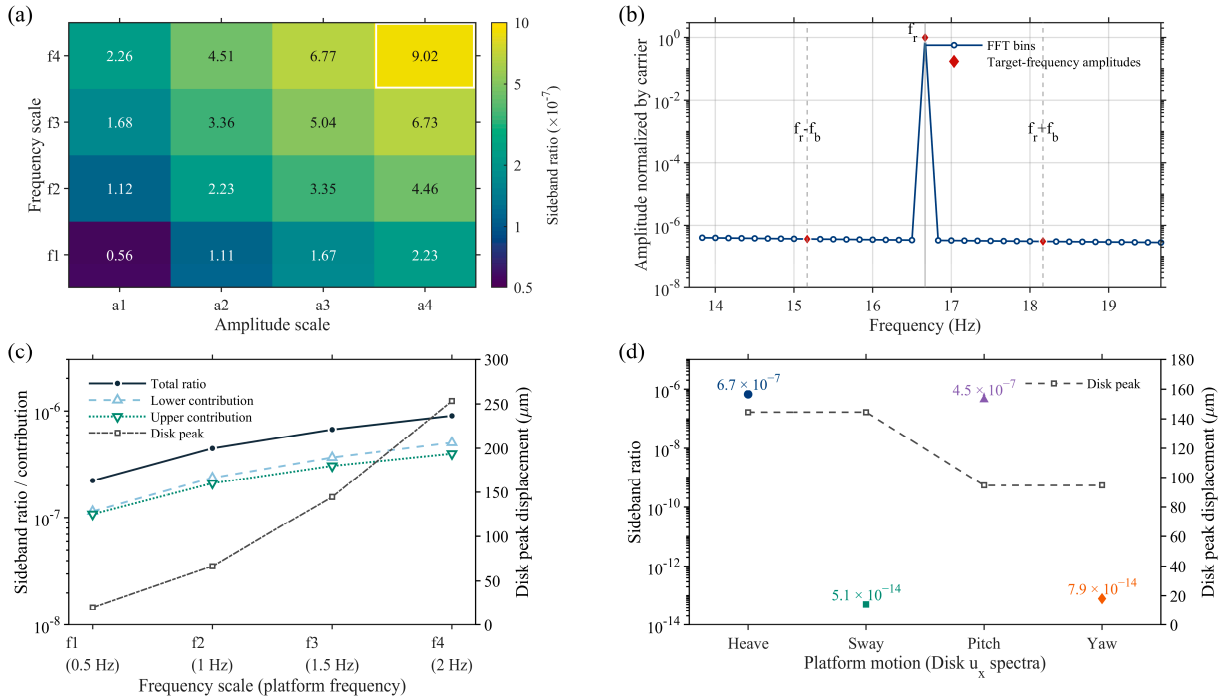


Figure 16. Steady-state spectra and spectral ratios of the disk u_x response at 1000 rpm, evaluated over $3 \leq t < 9$ s: (**a**) spectral ratio on the amplitude–frequency parameter plane under heave at 1000 rpm; (**b**) local normalized FFT near the rotational frequency and the target frequencies $f_r \pm f_b$ for the a4/f3 case; (**c**) spectral ratio and contributions at the upper and lower target frequencies at different frequency levels with a4 fixed, with the disk peak superimposed; and (**d**) comparison of the spectral ratio and disk peak among platform degrees of freedom under a4/f3. The disk peak is the maximum radial displacement over the same interval.

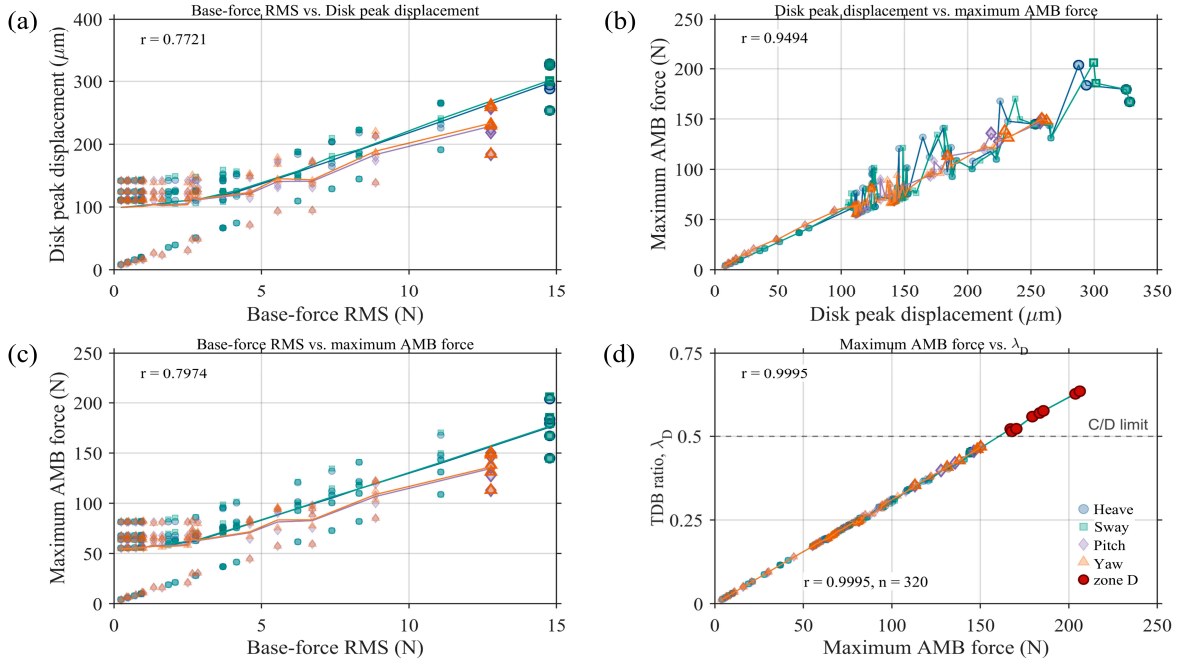


Figure 17. Pairwise relationships among the main variables for 320 discrete cases: (**a**) base-force RMS versus the disk peak; (**b**) disk peak versus the maximum AMB control force; (**c**) base-force RMS versus the maximum AMB control force; and (**d**) maximum AMB control force versus λ_D. The corresponding Pearson correlation coefficients are shown.

The three response metrics are taken at different locations and from different quantities: the disk peak from the radial displacement at the disk, the maximum AMB control force from the support feedback, and λ_D from the left and right support displacements relative to the minimum TDB clearance. Together, they describe global rotor deformation, control demand, and local clearance conditions.

5. Conclusions

The following conclusions are drawn from the closed-loop model of the ship-mounted flexible rotor–AMB system and the 320 discrete parameter cases.

1. The platform-induced response is quasi-static and superposes on the synchronous unbalance orbit. Stronger excitation makes the platform component dominant, which switches the dominant support from right to left and shifts the axial hotspot, while the response center and spatial width change little.
2. The left–right support relationship follows the TDB compliances: translational acceleration loads the left TDB more ($h_L > h_R$) and angular acceleration the right TDB ($e_R > e_L$), so heave and sway are left-dominated and pitch and yaw right-dominated.
3. Of the 320 cases, 256, 35, 19, and 10 fall in ISO 14839-2 zones A, B, C, and D, respectively; all zone-D cases occur under heave or sway, with a maximum λ_D of 0.635. The closed-form envelope ($R^2 = 0.997$) shows that the zone boundaries are hyperbolae $a_s f_s^2 = \Pi_\lambda(\Omega)$, and entering zone D requires 4.9–7.1 g, depending on rotational speed.
4. Increasing the frequency level amplifies λ_D and the AMB control force more than increasing the amplitude level, because the platform acceleration scales with $a_s f_s^2$ while the closed-loop compliance is practically frequency-independent below 2 Hz.
5. The maximum disk displacement occurs at 2500 rpm, whereas the maximum AMB control force and λ_D occur at 7000 rpm. The control force and λ_D are linearly related ($r = 0.9995$) because the integral and derivative actions of the PID controller are negligible at the platform frequencies.

Author Contributions: Conceptualization, H.W. and Z.W.; methodology, H.W.; software, H.W.; validation, L.H. and H.W.; formal analysis, Z.W.; investigation, W.S.; resources, W.S.; data curation, X.W.; writing—original draft preparation, H.W. and Z.W.; writing—review and editing, Z.W. All authors have read and agreed to the published version of the manuscript.

Funding: The research was supported by the Independent-sponsored Research Project of Naval University of Engineering.

Institutional Review Board Statement: Not applicable.

Informed Consent Statement: Not applicable.

Data Availability Statement: The original contributions presented in this study are included in the article. Further inquiries can be directed to the corresponding author.

Acknowledgments: The authors appreciate the constructive suggestions provided by the anonymous reviewers, which have significantly improved the quality of this paper. AI tools were used for proofreading and avoiding grammar errors.

Conflicts of Interest: The authors declare no conflicts of interest.

References

1. Siva Srinivas, R.; Tiwari, R.; Kannababu, C. Application of active magnetic bearings in flexible rotordynamic systems—A state-of-the-art review. *Mech. Syst. Signal Process.* **2018**, *106*, 537–572. [CrossRef]
2. Dutta, D.; Kumar Biswas, P.; Debnath, S.; Ahmad, F. Advancements and challenges in active magnetic bearings: A comprehensive review of performance, control, and future prospects. *IEEE Access* **2025**, *13*, 3051–3071. [CrossRef]

3. Cole, M.O.T.; Keogh, P.S.; Burrows, C.R. Vibration control of a flexible rotor/magnetic bearing system subject to direct forcing and base motion disturbances. *Proc. Inst. Mech. Eng. Part C J. Mech. Eng. Sci.* **1998**, *212*, 535–546. [CrossRef]
4. Das, A.S.; Dutt, J.K.; Ray, K. Active vibration control of unbalanced flexible rotor–shaft systems parametrically excited due to base motion. *Appl. Math. Model.* **2010**, *34*, 2353–2369. [CrossRef]
5. Soni, T.; Das, A.S.; Dutt, J.K. Active vibration control of ship mounted flexible rotor-shaft-bearing system during seakeeping. *J. Sound Vib.* **2020**, *467*, 115046. [CrossRef]
6. Zhang, G.; Liu, S.; Ma, R.; Liu, Z. Nonlinear dynamic characteristics of journal bearing–rotor system considering the pitching and rolling motion for marine turbo machinery. *Proc. Inst. Mech. Eng. Part M J. Eng. Marit. Environ.* **2015**, *229*, 95–107. [CrossRef]
7. Dakel, M.; Baguet, S.; Dufour, R. Steady-state dynamic behavior of an on-board rotor under combined base motions. *J. Vib. Control* **2014**, *20*, 2254–2287. [CrossRef]
8. Han, Y.; Li, M. Nonlinear dynamic characteristics of marine rotor-bearing system under heaving motion. *Shock Vib.* **2019**, *2019*, 7683952. [CrossRef]
9. Zhang, W.; Li, M. Nonlinear dynamic characteristics of marine rotor-bearing system under coupled heave and pitch ship motions. *Proc. Inst. Mech. Eng. Part C J. Mech. Eng. Sci.* **2022**, *236*, 63–79. [CrossRef]
10. Xie, X.; Li, M.; Du, X. Nonlinear dynamics of marine rotor-bearing system coupled with vibration isolation structure subject to ship rolling motion. *Appl. Math. Model.* **2022**, *103*, 344–359. [CrossRef]
11. Liu, Z.; Liu, Z.; Li, Y.; Zhang, G. Dynamics response of an on-board rotor supported on modified oil-film force considering base motion. *Proc. Inst. Mech. Eng. Part C J. Mech. Eng. Sci.* **2018**, *232*, 245–259. [CrossRef]
12. Bouziani, R.; Ouelaa, N. Simulation of the dynamic behavior of a rotor subject to base motion under variable rotational speed. *Mech. Ind.* **2017**, *18*, 308. [CrossRef]
13. Briend, Y.; Dakel, M.; Chatelet, E.; Andrianoely, M.-A.; Dufour, R.; Baudin, S. Effect of multi-frequency parametric excitations on the dynamics of on-board rotor-bearing systems. *Mech. Mach. Theory* **2020**, *145*, 103660. [CrossRef]
14. Soni, T.; Dutt, J.K.; Das, A.S. Parametric stability analysis of active magnetic bearing supported rotor system with a novel control law subject to periodic base motion. *IEEE Trans. Ind. Electron.* **2020**, *67*, 1160–1170. [CrossRef]
15. Xu, Y.; Shen, Q.; Zhang, Y.; Zhou, J.; Jin, C. Dynamic modeling of the active magnetic bearing system operating in base motion condition. *IEEE Access* **2020**, *8*, 166003–166013. [CrossRef]
16. Zhang, Y.; Zhou, J.; Zhang, Y.; Zhou, Y.; Xu, Y. Modelling and vibration response of a magnetically suspended flexible rotor considering base motion. *Appl. Math. Model.* **2023**, *118*, 518–540. [CrossRef]
17. Zhang, Y.; Xu, Y.; Zhou, J.; Zhou, Y.; Mahfoud, J. Vibration control of AMB-rotor system under base motions based on disturbance observer. *IEEE/ASME Trans. Mechatron.* **2025**, *30*, 5398–5407. [CrossRef]
18. Jang, M.-J.; Chen, C.-L.; Tsao, Y.-M. Sliding mode control for active magnetic bearing system with flexible rotor. *J. Frankl. Inst.* **2005**, *342*, 401–419. [CrossRef]
19. Tanaka, N.; Uchiyama, N.; Watanabe, T.; Seto, K. Levitation and vibration control of a flexible rotor by using active magnetic bearing. *J. Syst. Des. Dyn.* **2009**, *3*, 551–562. [CrossRef]
20. Xu, F.; Wang, J.; Zhu, K.; Wang, G.; Yi, J.; Xie, Z. Experimental study on vibration characteristics of journal bearing-rotor system under base roll and pitch motions. *Lubricants* **2025**, *13*, 242. [CrossRef]
21. Zhang, X.; Liu, Y.; Wang, Q.; Xing, Z.; Li, M. Numerical simulation and experimental study on dynamic characteristics of gas turbine rotor system subjected to ship hull excitation. *Processes* **2024**, *12*, 2091. [CrossRef]
22. Zhang, B.; Chen, X.; Xiang, F.; Ren, G.; Gan, X. Dynamic characteristics and periodic stability analysis of rotor system with squeeze film damper under base motions. *Appl. Sci.* **2025**, *15*, 1186. [CrossRef]
23. Singh, S.S.; Kumar, P. Vibration control in a co-rotating twin-spool rotor system under base excitation and mass unbalance using active magnetic bearings. *J. Vib. Eng. Technol.* **2024**, *12*, 2067–2090. [CrossRef]
24. Lal, M.; Kumar, K.S.; Gautam, A.K. Characteristic parameters assessment of AMB and PID controller used in vibration control of base-excited rotors. *J. Inst. Eng. India Ser. C* **2026**, *107*, 1383–1399. [CrossRef]
25. Zeng, Y.; Xiao, P.; Wei, J. Dynamic characteristics and feedforward control methods of magnetic bearing flywheels under moving base conditions. *Appl. Sci.* **2026**, *16*, 3789. [CrossRef]
26. Jarroux, C.; Mahfoud, J.; Dufour, R.; Legrand, F.; Defoy, B.; Alban, T. Investigations on the dynamic behaviour of an on-board rotor-AMB system with touchdown bearing contacts: Modelling and experimentation. *Mech. Syst. Signal Process.* **2021**, *159*, 107787. [CrossRef]
27. Keogh, P.S.; Cole, M.O.T. Rotor vibration with auxiliary bearing contact in magnetic bearing systems. Part 1: Synchronous dynamics. *Proc. Inst. Mech. Eng. Part C J. Mech. Eng. Sci.* **2003**, *217*, 377–392. [CrossRef]
28. Cole, M.O.T.; Keogh, P.S. Rotor vibration with auxiliary bearing contact in magnetic bearing systems. Part 2: Robust synchronous control for rotor position recovery. *Proc. Inst. Mech. Eng. Part C J. Mech. Eng. Sci.* **2003**, *217*, 393–409. [CrossRef]
29. Zeng, S. Modelling and experimental study of the transient response of an active magnetic bearing rotor during rotor drop on back-up bearings. *Proc. Inst. Mech. Eng. Part I J. Syst. Control Eng.* **2003**, *217*, 505–517. [CrossRef]

30. Zeng, S.; Zhang, J.-Q.; Wang, H.-N. Transient response of active magnetic bearing rotor during rotor drop on backup bearings. *Proc. Inst. Mech. Eng. Part C J. Mech. Eng. Sci.* **2006**, *220*, 785–794. [CrossRef]
31. Sun, G. Rotor drop and following thermal growth simulations using detailed auxiliary bearing and damper models. *J. Sound Vib.* **2006**, *289*, 334–359. [CrossRef]
32. Keogh, P.S.; Yong, W.Y. Thermal assessment of dynamic rotor/auxiliary bearing contact events. *J. Tribol.* **2007**, *129*, 143–152. [CrossRef]
33. Sahinkaya, M.N.; Abulrub, A.-H.G.; Keogh, P.S.; Burrows, C.R. Multiple sliding and rolling contact dynamics for a flexible rotor/magnetic bearing system. *IEEE/ASME Trans. Mechatron.* **2007**, *12*, 179–189. [CrossRef]
34. Halminen, O.; Kärkkäinen, A.; Sopanen, J.; Mikkola, A. Active magnetic bearing-supported rotor with misaligned cageless backup bearings: A dropdown event simulation model. *Mech. Syst. Signal Process.* **2015**, *50–51*, 692–705. [CrossRef]
35. Saket, F.Y.; Sahinkaya, M.N.; Keogh, P.S. Measurement and calibration of rotor/touchdown bearing contact in active magnetic bearing systems. *Mech. Syst. Signal Process.* **2019**, *122*, 1–18. [CrossRef]
36. Saket, F.Y.; Keogh, P.S. Force-based feedforward control of persistent synchronous rotor/touchdown bearing contact in active magnetic bearing systems. *Mech. Syst. Signal Process.* **2023**, *201*, 110657. [CrossRef]
37. Ruhl, R.L.; Booker, J.F. A finite element model for distributed parameter turborotor systems. *J. Eng. Ind.* **1972**, *94*, 126–132. [CrossRef]
38. Nelson, H.D.; McVaugh, J.M. The dynamics of rotor-bearing systems using finite elements. *J. Eng. Ind.* **1976**, *98*, 593–600. [CrossRef]
39. Nelson, H.D. A finite rotating shaft element using Timoshenko beam theory. *J. Mech. Des.* **1980**, *102*, 793–803. [CrossRef]
40. Genta, G. *Dynamics of Rotating Systems*; Springer: New York, NY, USA, 2005.
41. Friswell, M.I.; Penny, J.E.T.; Garvey, S.D.; Lees, A.W. *Dynamics of Rotating Machines*; Cambridge University Press: Cambridge, UK, 2010. [CrossRef]
42. Lalanne, M.; Ferraris, G. *Rotordynamics Prediction in Engineering*, 2nd ed.; Wiley: Chichester, UK, 1998.
43. Shabana, A.A. *Dynamics of Multibody Systems*, 5th ed.; Cambridge University Press: Cambridge, UK, 2020. [CrossRef]
44. Schweitzer, G.; Maslen, E.H. (Eds.) *Magnetic Bearings: Theory, Design, and Application to Rotating Machinery*; Springer: Berlin/Heidelberg, Germany, 2009. [CrossRef]
45. Schweitzer, G.; Bleuler, H.; Traxler, A. *Active Magnetic Bearings: Basics, Properties and Applications of Active Magnetic Bearings*; vdf Hochschulverlag AG: Zurich, Switzerland, 1994.
46. Chiba, A.; Fukao, T.; Ichikawa, O.; Oshima, M.; Takemoto, M.; Dorrell, D.G. *Magnetic Bearings and Bearingless Drives*; Elsevier: Oxford, UK, 2005.
47. Newmark, N.M. A method of computation for structural dynamics. *J. Eng. Mech. Div.* **1959**, *85*, 67–94. [CrossRef]
48. Bathe, K.-J. *Finite Element Procedures*; Prentice Hall: Upper Saddle River, NJ, USA, 1996.
49. Harris, F.J. On the use of windows for harmonic analysis with the discrete Fourier transform. *Proc. IEEE* **1978**, *66*, 51–83. [CrossRef]
50. Oppenheim, A.V.; Schafer, R.W. *Discrete-Time Signal Processing*, 3rd ed.; Prentice Hall: Upper Saddle River, NJ, USA, 2009.
51. *ISO 14839-2:2004*; Mechanical Vibration—Vibration of Rotating Machinery Equipped with Active Magnetic Bearings—Part 2: Evaluation of Vibration. International Organization for Standardization: Geneva, Switzerland, 2004.
52. Bendat, J.S.; Piersol, A.G. *Random Data: Analysis and Measurement Procedures*, 4th ed.; Wiley: Hoboken, NJ, USA, 2010.

Disclaimer/Publisher's Note: The statements, opinions and data contained in all publications are solely those of the individual author(s) and contributor(s) and not of MDPI and/or the editor(s). MDPI and/or the editor(s) disclaim responsibility for any injury to people or property resulting from any ideas, methods, instructions or products referred to in the content.